Research Paper

GEOSPHERE

GEOSPHERE

https://doi.org/10.1130/GES02502.1

11 figures; 3 tables; 1 set of supplemental files

CORRESPONDENCE: jordanww@email.arizona.edu

CITATION: Wang, J.W., Gehrels, G., Kapp, P., and Sundell, K., 2022, Evidence for regionally continuous Early Cretaceous sinistral shear zones along the western flank of the Coast Mountains, coastal British Columbia, Canada: Geosphere, https://doi.org/10.1130/GES02502.1.

Science Editor: David E. Fastovsky
Associate Editor: Nancy Riggs

Received 5 December 2021
Revision received 14 June 2022
Accepted 5 September 2022

Published online 12 December 2022

Evidence for regionally continuous Early Cretaceous sinistral shear zones along the western flank of the Coast Mountains, coastal British Columbia, Canada

Jordan W. Wang[1], George Gehrels[1], Paul Kapp[1], and Kurt Sundell[2]

[1]Department of Geosciences, University of Arizona, Tucson, Arizona 85719, USA
[2]Department of Geosciences, Idaho State University, Pocatello, Idaho 83209, USA

ABSTRACT

The plate-boundary conditions of the Mesozoic North American Cordillera remain poorly constrained, but most studies support large (>800 km) southward motion of the Insular and Intermontane superterranes during Jurassic–Cretaceous time. An implicit feature in these models of large coastwise displacements is the presence of one or more continental-scale sinistral strike-slip faults that could have dismembered and displaced terrane fragments southward along the western margin of North America prior to the onset of mid-Cretaceous shortening and dextral strike-slip faulting. In this study, we documented a system of sinistral intra-arc shear zones within the Insular superterrane that may have accommodated large southward motion. Employment of a new large-*n* igneous zircon U-Pb method more than doubled the precision of measurements obtained by laser ablation–inductively coupled plasma–mass spectrometry (from ~1% to 0.5%) and allowed us to demonstrate the close temporal-spatial relationship between magmatism and deformation by dating comagmatic crosscutting phases. Crystallization ages of pre-, syn-, and postkinematic intrusions show that the intra-arc shear zones record an Early Cretaceous phase of sinistral oblique convergence that terminated between 107 and 101 Ma. Shear zone cessation coincided with: (1) collapse of the Gravina basin, (2) development of a single voluminous arc that stitched the Insular and Intermontane superterranes together, and (3) initiation of east-west contractional deformation throughout the Coast Mountains. We interpret these concurrent tectono-magmatic events to mark a shift in plate kinematics from a sinistral-oblique system involving separate terranes and intervening ocean basins to a strongly convergent two-plate margin involving a single oceanic plate and the newly assembled western margin of North America.

INTRODUCTION

The paleogeography and tectonic assembly of suspect terranes in the Mesozoic North American Cordillera remain some of the most controversial aspects of Cordilleran tectonics due to subduction of the paleo-Pacific oceanic rock record and overprinting complexities of younger faulting and magmatism. Sparse geologic and geochronologic data near key geologic boundaries have allowed the proliferation of several mutually exclusive models for the assembly of western North America, all with distinct timing, paleogeographic (Fig. 1), and tectonic associations that have unique implications for the development of the North American Cordillera. These models are numerous and varied but revolve around three current controversies in the Canadian Cordillera: (1) the polarity of subduction and facing direction of arc magmatism, (2) the timing of terrane assembly with the western margin, and (3) the lateral mobility of terranes during and after collision.

Jordan Wang https://orcid.org/0000-0003-1554-4062

A recent debate has focused on the polarity of subduction and arc magmatism in Jurassic–Cretaceous time, with several authors (most notably Sigloch and Mihalynuk, 2013, 2017; Clennett et al., 2020) challenging the long-standing paradigm of >180 m.y. of east-dipping subduction beneath North America to produce the Coast Mountains Batholith and other correlative along-strike arc segments (the Idaho Batholith, Sierra Nevada Batholith, Peninsular Range Batholith, etc.). The model proposed by Sigloch and Mihalynuk (2017) for west-dipping subduction and its derivatives suggests that the Mesozoic arc rocks of the northern Cordillera were formed as an island arc (the Insular superterrane) above a long-lived and stationary intra-oceanic subduction zone far away from the western margin of North America and were assembled with the western margin (the Intermontane superterrane) in the Early Cretaceous, presumably by thrust emplacement of an east-facing forearc assemblage over North American–affinity passive-margin strata or previously accreted terranes. Full examination of this model is beyond the scope of this paper, but we do note that thrust faults and related folds in the suture zone between the Insular and Intermontane superterranes verge west (dip east) and emplace high-grade rocks of North American affinity over arc rocks and associated basinal assemblages of the Insular superterrane, suggesting an overall east-dipping subduction-collision geometry (McClelland et al., 1992; Gehrels and Boghossian, 2000; Gehrels, 2001).

A second and long-standing controversy is the timing of collision between the Insular and Intermontane superterranes. Most workers agree that the Intermontane superterrane and associated

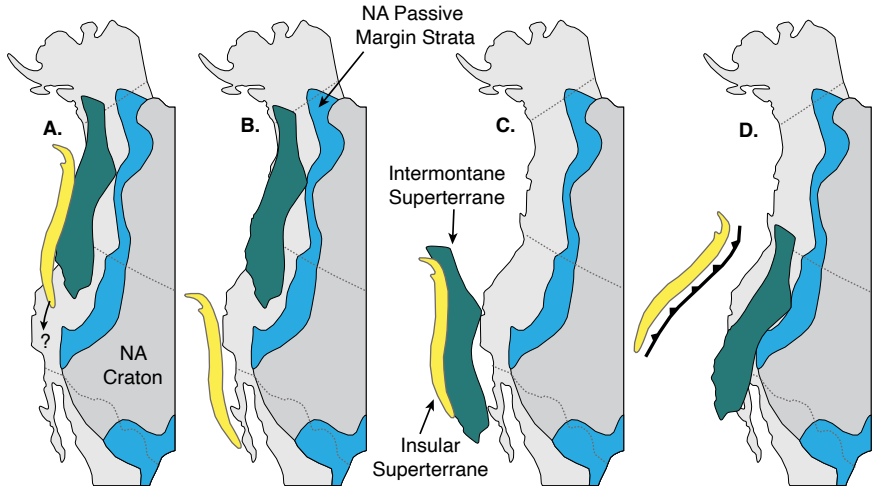

Figure 1. Tectonic cartoons depicting end-member models for Cretaceous paleogeography. NA—North America. (A) Restoration of dextral offset on Cretaceous–Paleogene faults. (B) Classic Baja–British Columbia (BC) hypothesis based on paleomagnetic (Cowan et al., 1997), biogeographic (Miller et al., 2006), and detrital zircon (Garver and Davidson, 2015; Matthews et al., 2017) data from the Insular superterrane. (C) Revised Baja-BC (or "Cordillera") reconstruction based on paleomagnetic data from both the Insular and Intermontane superterranes (Enkin, 2006). (D) East-facing subduction zone between the Insular and Intermontane superterranes during Jurassic–Cretaceous time (e.g., Sigloch and Mihalynuk, 2013, 2017).

pre–Middle Jurassic arc terranes in the U.S. Cordillera were built on basement that was accreted to the western margin of North America by Late Triassic or Middle Jurassic time in a west-dipping subduction-collision geometry (Monger, 2014; Sigloch and Mihalynuk, 2017; Pavlis et al., 2019). However, there is disagreement about whether the Insular-Intermontane collision initiated during latest Triassic to Middle Jurassic (McClelland and Gehrels, 1990; van der Heyden, 1992; Gehrels, 2001; Monger et al., 2006; Monger, 2014) or mid-Cretaceous time (Monger et al., 1982; Rubin et al., 1990; McGroder, 1991; Monger, 2014; Sigloch and Mihalynuk, 2017). Models for Early Jurassic collision of the Insular and Intermontane superterranes are based on potential Jurassic overlap sequences and stitching plutons that are interpreted to tie rocks of the Insular and Intermontane superterranes by 170–164 Ma (e.g., Gehrels, 2001; Monger et al., 2006). In these Early Jurassic collision models, Late Jurassic to Early Cretaceous basinal assemblages would be the remnants of postcollisional backarc rifts (i.e., the Kahiltna, Nutzotin, Gravina, and Tyaughton-Methow basins), which opened along the approximate boundary of the original suture and were closed and inverted during mid-Cretaceous regional contraction in the Coast Mountains of southeast Alaska and British Columbia (e.g., van der Heyden, 1992). The issue with models for initial Jurassic collision is that Jurassic volcanic and plutonic rocks are nonunique in the North American Cordillera, and not enough geochemical or structural-stratigraphic work has been published to demonstrate that these units are correlative across the Coast Mountains and truly "overlap" or "stitch" rocks belonging to the Insular and Intermontane superterranes (see Sigloch and Mihalynuk, 2017, their section 3.3.3). Thus, more conservative models for the Insular-Intermontane collision posit that the Insular superterrane did not collide with the western margin of the Intermontane superterrane until mid-Cretaceous time, when clear overlap sequences, unambiguous stitching plutons, and widespread contraction in the suture zone between the two terranes were established (e.g., Monger et al., 1982; McGroder, 1991; Sigloch and Mihalynuk, 2017). Because it is not clear which of these models is correct in our study area, and because this study focused on Cretaceous tectonics of the Coast Mountains, we will refer to the mid-Cretaceous event that definitively tied the Insular and Intermontane superterranes together as "terminal suturing" rather than "collision" to allow for the large uncertainty in collision timing in the region.

A third controversy, and the focus of this article, centers around the lateral mobility of terranes in the northern Cordillera. Paleomagnetic and biogeographic data sets suggest that the Insular and Intermontane superterranes were displaced >1500 km southward (relative to North America) during Jurassic–Early Cretaceous time, and then they moved back northward by at least the same amount during Late Cretaceous–Paleogene time (Fig. 2; Beck, 1991; Cowan et al., 1997; Carter and Haggart, 2006; Enkin, 2006; Miller et al., 2006). The later northward translation of terranes has been the subject of vigorous debate for the past several decades and is generally referred to as the "Baja-BC" controversy, based on the original hypothesis that the Insular superterrane originated up to 3000 km south of its present position in British Columbia (BC) near present-day Baja California, based on paleomagnetic data sets (Cowan et al., 1997). More recent paleomagnetic constraints show that Late Cretaceous rocks assigned to the Intermontane superterrane also have anomalously shallow magnetic inclinations, leading to a revised Baja-BC hypothesis that suggests the Insular and Intermontane superterranes have been at the same latitudes since at least the Early Cretaceous and were translated to the south during mid-Cretaceous time (ca. 110–85 Ma) and then back north during Late Cretaceous to Paleogene time (Fig. 2; Enkin, 2006). Up to 1000 km of Jurassic–Early Cretaceous sinistral displacement is also proposed to have occurred within and/or between the Intermontane and Insular superterranes prior to Baja-BC–related motion (e.g., Monger et al., 1994; Umhoefer et al., 2002, 2006; Umhoefer, 2003; Gehrels et al., 2009; Anderson, 2015; Yokelson et al., 2015). Although

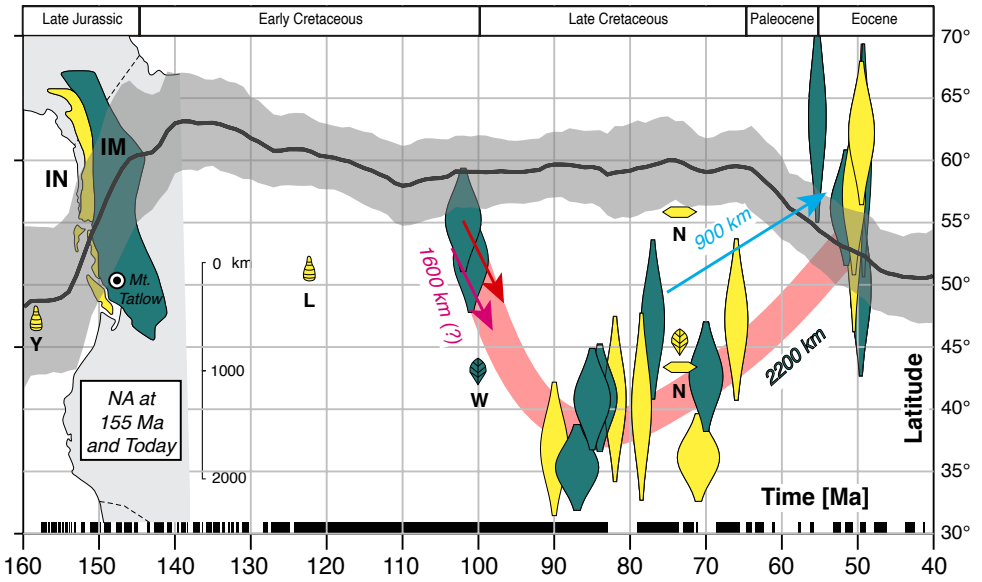

Figure 2. Evidence for south-then-north translation of Insular (IN) and Intermontane (IM) terranes, adapted from Enkin (2006). Solid black curve shows latitudinal motion of North America (NA) inferred from global data set of paleomagnetic poles for cratons; gray bounding area shows 95% confidence (from Enkin, 2006). Lozenges show paleomagnetic data with latitudinal errors for bedded rocks of the Insular and Intermontane superterranes (Enkin, 2006). Paleolatitudes of the Yakoun Group (Y) and Longarm Formation (L; Carter and Haggart, 2006), Winthrop Formation (W; Miller et al., 2006), and Nanaimo Group (N; Pearson and Hebda, 2006) are from biogeographic information. Hexagonal yellow paleolatitude estimates of the Nanaimo Group (N; Mahoney et al., 1999; Mathews et al., 2017) are from detrital zircon data. Dextral offsets on known faults (blue arrow) are from Wyld et al. (2006). Evidence for sinistral translation (red arrows) is referenced in the text. All information has been referenced to show paleoposition of Mount Tatlow (51.3°N, 123.8°W; following Enkin, 2006). The global polarity time scale is plotted along the bottom, with black being normal and white being reverse magnetic polarity.

much attention has been devoted to the Late Cretaceous to Paleogene dextral displacements in the past few decades, relatively little work has focused on the earlier phase(s) of hypothesized sinistral displacements.

This study was motivated by evidence for 600–1000 km of sinistral displacement within the Insular superterrane. Paleomagnetic data indicate major post-Triassic sinistral dismemberment of Wrangellia (part of Insular superterrane), with the Vancouver Island portion (Fig. 3) having been displaced from the southern Alaskan portion by ~15° of latitude (~600–1000 km; Plafker et al., 1989; Plafker and Berg, 1994). Tochilin et al. (2014) argued for ~1000 km of Jurassic–Cretaceous sinistral offset between the Banks Island assemblage of the Insular superterrane and similar Lower Paleozoic continental margin strata in the Saint Elias Mountains of Alaska. Chardon et al. (1999) suggested that sinistral shear zones in the midcoast region of British Columbia accommodated significant translations based on the separation of different-aged plutons and regional foliation deflection patterns, but they did not provide displacement magnitude estimates.

The period of hypothesized sinistral translation coincides with major intrusive episodes along the eastern margin of the Insular superterrane in the western Coast Mountains Batholith, suggesting that southward coastwise terrane transport (if any) was accomplished in a setting of sinistral-oblique convergence. Modern and ancient arcs in obliquely convergent settings are characterized by intra-arc shear zones, where the thermally weak arc accommodates transpressional strain with varying degrees of strike-slip partitioning (Tikoff and Teyssier, 1994; Tikoff and Greene, 1997; de Saint Blanquat et al., 1998). In these intra-arc transpressional settings, magmatism and deformation are closely linked (e.g., Hutton, 1988; D'Iemos et al., 1992; Hutton and Reavy, 1992; Neves et al., 1996; de Saint Blanquat and Tikoff, 1997; Hutton, 1997), and the precise timing of transpressional strain may be constrained by dating syntectonic intrusions that record magmatic-state (i.e., hypersolidus, "pre–full crystallization," "primary," etc.) deformation.

In this study, we investigated the timing and synmagmatic nature of a system of interlinked sinistral shear zones localized in the western Coast Mountains Batholith of the Insular superterrane (Fig. 3). Although the data we present provide important constraints on collision and mid-Cretaceous plate kinematics, the goal of this article is not to falsify or identify a preferred model for the assembly of the Cordilleran collage. Instead, we provide plate-kinematic constraints for a critical time interval (ca. 120–100 Ma) in the Canadian Cordillera by integrating zircon U-Pb geochronology with a qualitative strain analysis of arc rocks from the western Coast Mountains Batholith. New geologic mapping of shoreline exposures between the coastal towns of Kitkatla and Klemtu (~54°N–52°N; Fig. 4) extends the southernmost known trace of sinistral shear zones in the western Coast Mountains Batholith by >100 km. In an effort to generate the tightest possible age constraints, we implemented a new routine for large-*n* igneous zircon U-Pb geochronology by laser ablation–inductively coupled plasma–mass spectrometry (LA-ICP-MS) that improved the precision of weighted mean crystallization ages (from ~1%–2% to ~0.5%) by leveraging the power of counting statistics. Crystallization ages of pre-,

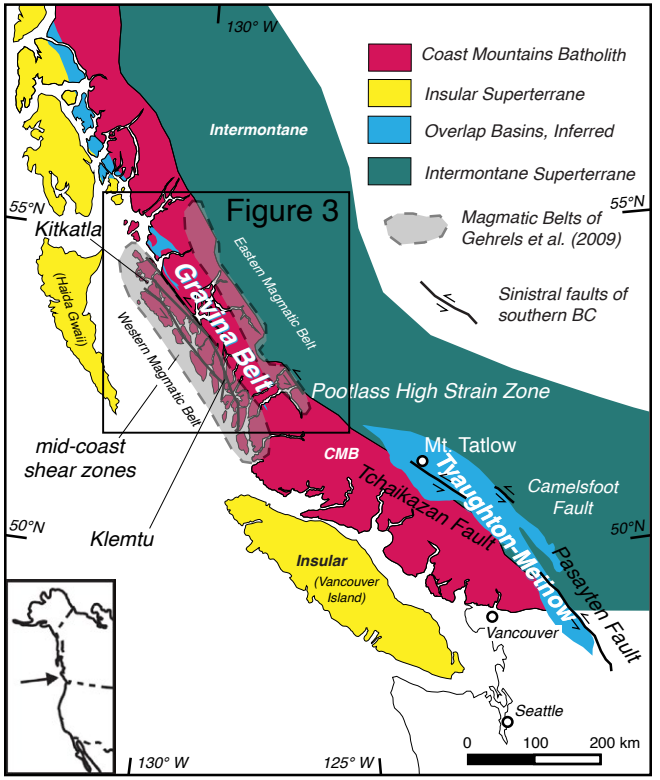

Figure 3. Generalized terrane map of British Columbia (BC) highlighting superterranes, magmatic belts described by Gehrels et al. (2009), Jurassic–Cretaceous basins, and mid-Cretaceous sinistral faults of the Tyaughton-Methow realm. Late Cretaceous to Eocene dextral strike-slip faults are not included for simplicity. CMB—Coast Mountains Batholith. Figure is modified from Rusmore et al. (2013).

syn-, and postkinematic intrusions from seven localities over a 250-km-long strike length show that regional sinistral shear zone deformation in the western Coast Mountains Batholith developed synmagmatically, was active by at least 113 Ma, and terminated by 100 Ma. These new timing and petrographic results suggest that (1) sinistral shear zone deformation in the midcoast was the result of strike-slip partitioning in a growing magmatic arc during oblique convergence, (2) the intra-arc shear zones of the midcoast likely did not accommodate the full 800 km of hypothesized left-lateral displacement, (3) sinistral deformation in the Coast Mountains immediately preceded 100–90 Ma regional contraction, and (4) the Insular and Intermontane superterranes were kinematically linked by at least ca. 113 Ma.

GEOLOGIC SETTING

This study is focused on the geology of coastal British Columbia between the towns of Kitkatla to the north and Klemtu to the south (~54°N–52°N; Fig. 4), herein referred to as the midcoast region. It includes the Insular superterrane in the west and the Intermontane superterrane to the east (as defined by Monger et al., 1982), which are locally overlain and separated by Upper Jurassic–Lower Cretaceous (meta)sedimentary rocks of the Gravina belt (Figs. 3 and 4; Wheeler and McFeely, 1991). At these latitudes, the Coast Mountains Batholith straddles and intrudes the tectonic boundary between the Insular and Intermontane superterranes and provides key age constraints on the history of terrane assembly in the North American Cordillera.

Coast Mountains Batholith

The Coast Mountains Batholith is a 1700-km-long magmatic-arc province that extends from northern Washington through southeastern Alaska and British Columbia to Yukon and eastern Alaska. Compilations of large U-Th-Pb zircon and titanite data sets show that the midcoast Coast Mountains Batholith comprises at least three distinct plutonic belts that are defined by the terranes into which they intrude and the relative timing of magmatic-arc flare-ups (Gehrels et al., 2009; Cecil et al., 2018):

(1) The western magmatic belt (Fig. 3) was mainly emplaced in rocks of the outboard Insular superterrane and was active 177–162 Ma, 157–142 Ma, and 118–100 Ma. In the study area (Fig. 4), tonalitic plutons of the western Coast Mountains Batholith intrude, and preserve in screens and pendants, metasedimentary rocks of the Alexander terrane. Plutons decrease in age from west to east, with Middle to Late Jurassic plutons intruding the Banks Island assemblage(?) and Early to middle Cretaceous plutons intruding rocks of the eastern Alexander terrane(?) near the Grenville Channel (Fig. 4). The depth of emplacement of the Late Jurassic–Early Cretaceous plutons increases from ~10 km in the west to ~25 km in the east (Butler et al., 2006).

(2) The eastern magmatic belt (Fig. 3) was mainly emplaced in rocks of the inboard Intermontane superterrane and was active continuously from 180 to 110 Ma. To the east of the study area, plutons of the eastern Coast Mountains Batholith intrude metavolcanic rocks of the Stikine terrane (Rusmore and Woodsworth, 1991). In contrast to the western Coast Mountains Batholith, plutons generally decrease in age from east to west (Gehrels et al., 2009). The eastern Coast Mountains Batholith is separated from the western Coast Mountains Batholith by Upper Jurassic–Lower Cretaceous strata of the Gravina belt (Fig. 4).

(3) The "overlap" magmatic belt ("post–100 Ma" intrusions of Fig. 4) records continuous magmatism from 100 to 50 Ma, overprints both the western and eastern belts, and systematically decreases

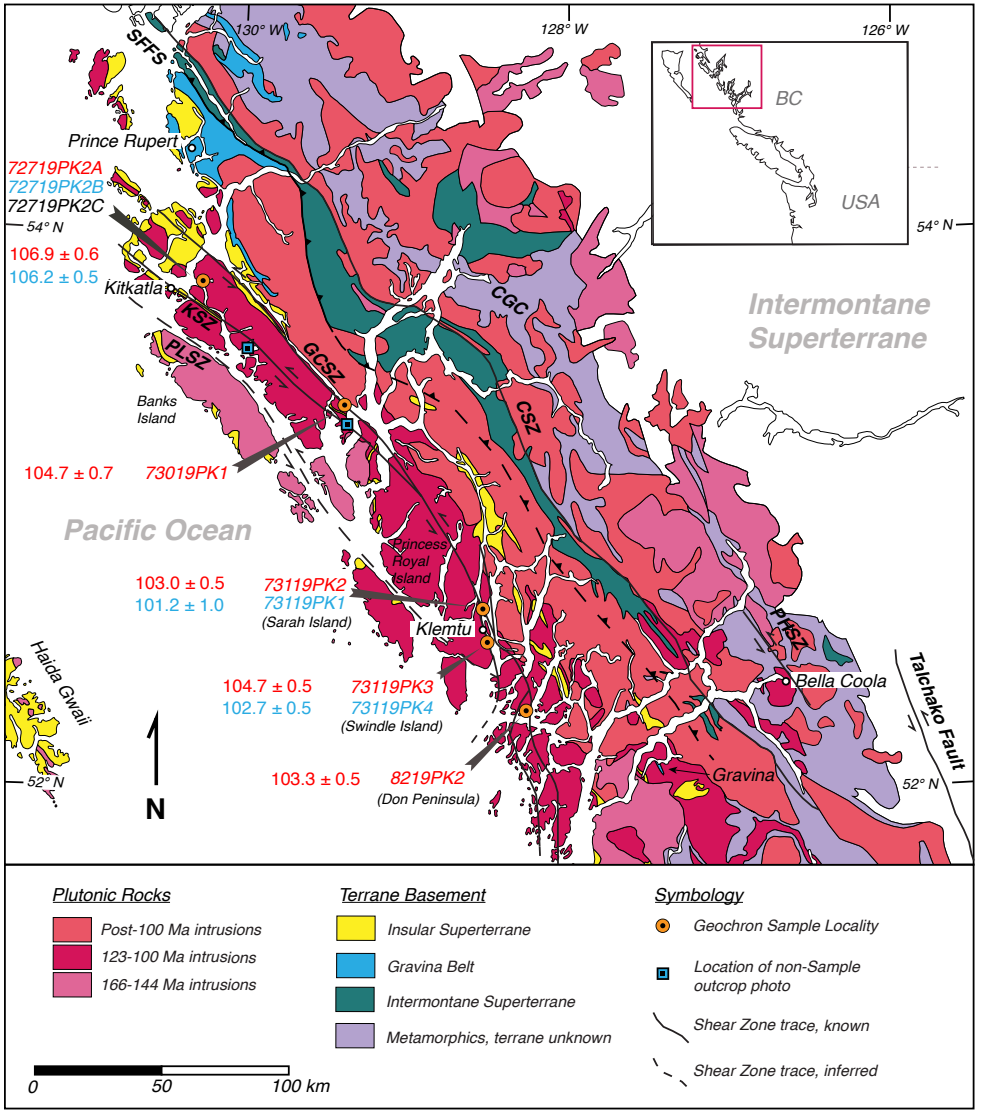

Figure 4. Terrane map of the midcoast region, British Columbia (BC), highlighting distribution of Jurassic–Cretaceous magmatism and major faults. Sample info in red—mylonitized tonalites; sample info in blue—crosscutting dikes. PLSZ—Principe Laredo shear zone; KSZ—Kitkatla shear zone; GCSZ—Grenville Channel shear zone; CSZ—Coast shear zone; PHSZ—Pootlass high-strain zone; CGC—Central gneiss complex; SFFS—Sumdum-Fanshaw fault system. Uncolored mainland is mostly Intermontane superterrane. Figure is adapted from Wheeler and McFeely (1991), Nelson et al. (2014), Gehrels and Boghossian (2000), and Cui et al. (2017).

in age to the east (~2 km/m.y.; Gehrels et al., 2009). Overlap intrusions in the study area are exposed on the northeastern shores of the Grenville Channel (Fig. 4), where they deflect older shear zone fabrics due to ballooning during shallow crustal emplacement (Chardon et al., 1999; Wolf et al., 2010). In many areas, voluminous post–100 Ma intrusions obscure the contacts between rocks of the Insular superterrane, Intermontane superterrane, and Gravina belt.

This architectural framework is valid in the midcoast region, where the western and eastern belts are separated by rocks of the Gravina belt (Figs. 2 and 3). It breaks down ~65 km to the southeast of the study area (Figs. 3 and 4), where 180 to 50 Ma magmatism shows no systematic spatial variations in age (Rusmore et al., 2013; Cecil et al., 2018). Detrital zircon studies of metasedimentary screens and roof pendants within the southern batholith have also proven to be inconclusive in determining the terrane affinity of host basement rocks (Insular vs. Gravina vs. Intermontane; Rusmore et al., 2013; Dafov et al., 2020).

Gravina Belt

Upper Jurassic to Lower Cretaceous volcanic and sedimentary rocks of the Gravina belt extend along the length of southeastern Alaska and continue southward to the British Columbia midcoast, ~66 km southwest of Bella Coola (Fig. 4). In southeastern Alaska, coherent stratigraphic sections of the Gravina belt depositionally overlie rocks of the Alexander (Insular) terrane in the west and Taku/Yukon-Tanana (Intermontane) terranes in the east (Berg et al., 1972). U-Pb detrital zircon studies have constrained the age of deposition to ca. 151–105 Ma, with a dominant western Coast Mountains Batholith/Insular terrane provenance (Kapp and Gehrels, 1998; Yokelson et al., 2015). The Gravina belt in the midcoast region is metamorphosed, transposed in west-vergent shear zones, and separates plutonic rocks of the western and eastern Coast Mountains Batholith (McClelland et al., 1992; Yokelson et al., 2015).

Midcoast Shear Zones

The approximately NW-SE–striking Kitkatla and Grenville Channel sinistral strike-slip shear zones are localized within plutonic rocks of the mid-Cretaceous western Coast Mountains Batholith (Fig. 3) and generally exhibit steeply dipping foliations, shallowly plunging mineral lineations, and sinistral sense-of-shear indicators, including S-C-C′ fabrics in mylonites, σ-clasts, asymmetric boudin structures, asymmetric fold structures, and fragmented porphyroclasts (Chardon et al., 1999; Nelson et al., 2011, 2012, 2014; Angen et al., 2014). Together, they define an ~30-km-wide, 250-km-long system of intra-arc transpressional and transtensional shear zones that variably record horizontal compression/tension and left-lateral motion during mid-Cretaceous time (Chardon, 2003; Nelson et al., 2011).

Previous geochronologic studies on the Kitkatla shear zone constrained the age of ductile deformation to between ca. 119 and 107 Ma. Butler et al. (2006) reported zircon U-Pb ages of 113 ± 4 Ma for a late kinematic (weakly deformed) quartz diorite that intrudes the western part of the Kitkatla shear zone and 107.5 ± 1.5 Ma for a granodiorite dike that cuts across the shear zone fabric ~9 km southeast of Kitkatla (near our samples 72719PK2A and 72719PK2B; Fig. 4). A similar timing for shear zone deformation ~24 km farther to the north is suggested where a metaconglomerate that may have been deposited in a transtensional basin associated with the Kitkatla shear zone yielded a maximum depositional age of ca. 119 Ma (based on the age of deformed granitic clasts) and is crosscut by an undeformed ca. 107 Ma pluton (Tochilin et al., 2014).

Previous work on the Grenville Channel shear zone yielded age estimates for fault motion ranging from 123 to 94 Ma. The northern portion of the Grenville Channel shear zone was active between 108 and 97 Ma, based on Lu-Hf ages of synkinematic garnet and zircon U-Pb ages of synkinematic dikes (Wolf et al., 2010; Angen et al., 2014). The southern portion of the Grenville Channel shear zone near Klemtu was mapped by Nelson et al. (2011); they reported zircon U-Pb ages for "synkinematic" intrusions ranging from 123 to 105 Ma, but it should be noted that the criteria for their interpretations of what constitutes pre-, syn-, and postkinematic intrusions are uncertain, and textural or petrographic information that could be used to distinguish subsolidus versus hypersolidus deformation is not currently available.

The Principe-Laredo fault is an approximately NW-SE–striking subvertical shear zone ~13 km to the west of the Kitkatla shear zone that is interpreted to be a part of the same (Kitkatla and Grenville Channel) sinistral shear zone system, based on deflection of regional foliation patterns (Chardon et al., 1999). It separates Middle Jurassic intrusions in the west on Banks Island from Early to middle Cretaceous intrusions in the east. Brittle deformation fabrics within the fault zone indicate younger overprinting by dextral strike-slip motion (Chardon et al., 1999).

GEOLOGIC MAPPING, STRUCTURAL ANALYSIS, AND SAMPLE DESCRIPTIONS

New shoreline mapping of sinistral shear zone fabrics extends the southern known trace of the sinistral fault system by >250 km from Klemtu to the southern tip of Don Peninsula and extends the southern trace of the Kitkatla shear zone by >100 km to Princess Royal Island, where it merges with the Grenville Channel shear zone (Fig. 4). Shear zone fabrics and sample descriptions are given from north to south, starting near Kitkatla.

Kitkatla Shear Zone Samples and Observations

Three samples from the Captain Cove plutonic suite were collected 9 km east of Kitkatla (Fig. 4) to determine age relations between deformed tonalites and undeformed crosscutting pegmatites at a single outcrop within the eastern part of the Kitkatla shear zone. The shear zone at this locality is characterized by a NW-striking and steeply NE-dipping (~60°) foliation and shallowly to moderately plunging (~12°–51°) mineral lineations that trend NNW-SSE. Sample 72719PK2A is a foliated and lineated biotite-hornblende tonalite that exhibits sinistral sense-of-shear indicators. Sample 72719PK2B is a synkinematic biotite-granitoid dike that crosscuts the deformed tonalite (Fig. 5A). Sample 72719PK2C is a fine-grained, weakly foliated, K-feldspar–rich leucocratic dike that crosscuts both the mylonitized host rock and the synkinematic dike.

Newly recognized shoreline exposures ~9 km northeast of the Principe-Laredo shear zone extend the known trace of the Kitkatla shear zone by >100 km to the southeast (Fig. 4). The shear zone fabric at these localities is expressed by a well-defined subvertical foliation (~315°, 86°) and mineral lineations that plunge shallowly to the NW and SE (Fig. 6A). Mylonitized tonalites have S-C-C′ fabrics and sigmoidal mafic enclaves showing sinistral sense-of-shear (Figs. 6B and 6C). Near southern Grenville Channel, the Kitkatla shear zone crops out within ~4 km of the Grenville Channel shear zone and displays mesoscale σ-clasts showing sinistral sense-of-shear (Figs. 4 and 6D).

Grenville Channel Shear Zone Sample and Observations

Sample 73019PK1 is a mylonitized garnet-bearing granite within the Grenville Channel shear zone (Fig. 3). Rotated garnets with recrystallized mica tails show sinistral sense-of-shear in thin section (Fig. 7A). Shear zone foliations at this locality dip steeply to the NE (294°, 69°) and exhibit mineral lineations defined by aligned hornblende that plunge moderately to the NW (314°, 41°).

Klemtu Samples and Observations (Southern Grenville Channel Shear Zone)

Six samples were collected from the southern Grenville Channel shear zone near Klemtu to determine age relationships between deformed tonalites and syn- to postkinematic dikes at three localities over an along-strike distance of 50 km (Fig. 4). The geology of the three locations is described from north to south.

Sample 73119PK2 is a mylonitized tonalite from the southwest shore of Sarah Island that displays

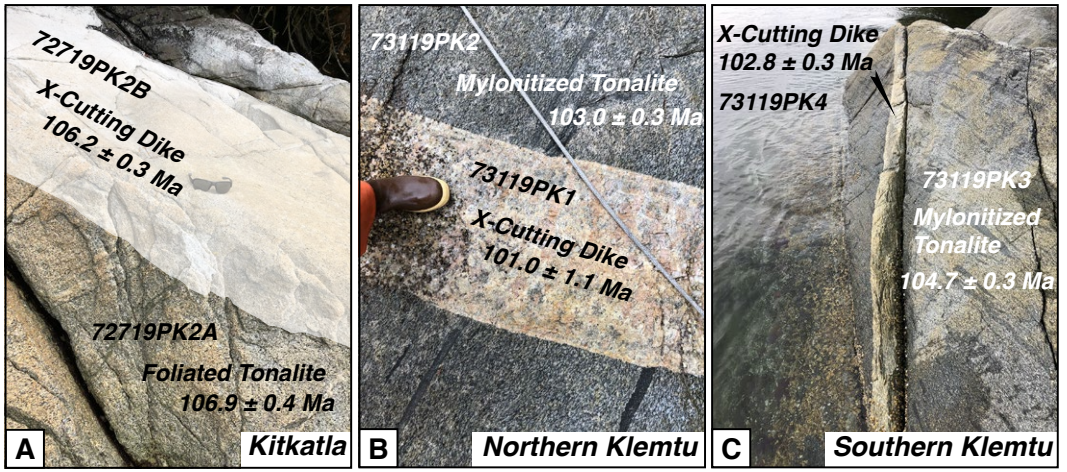

Figure 5. Annotated outcrop photos showing crosscutting ages at three localities along the Kitkatla and Grenville Channel shear zones. (A) Foliated tonalite crosscut (X-cut) by weakly deformed synkinematic biotite-granitoid dike in Beaver passage, eastern Kitkatla shear zone (53°46′1.96″N, 130°18′27.7″W). (B) Mylonitized tonalite with stretched and flattened mafic enclaves crosscut by undeformed postkinematic dike ~8 km northeast of Klemtu, southern Grenville Channel shear zone (52°39′45.12″N, 128°31′50.249″W). (C) Mylonitized tonalite with stretched and flattened mafic enclaves crosscut by weakly deformed biotite-granitoid dike 6 km southwest of Klemtu, southern Grenville Channel shear zone (52°32′23.039″N, 128°29′40.279″W).

sinistral S-C fabrics and abundant stretched mafic enclaves (Figs. 3 and 5E). Sample 73119PK1 is an undeformed K-feldspar–rich pegmatite dike from the same outcrop that crosscuts the host-rock mylonitic fabrics (Fig. 5B). The shear zone foliation at this locality is subvertical (329, 89), and the mineral lineation plunges shallowly to the NW (317, 11). Near Klemtu, finely spaced S-C fabrics and smaller grain sizes in mylonitized tonalites mark the central part of the shear zone, where deformation is greatest (Fig. 6F).

Sample 73119PK3 is a mylonitized hornblende-biotite tonalite from the eastern shore of Swindle Island (Fig. 4) that displays sinistral S-C fabrics and abundant mafic enclaves stretched parallel to the foliation fabric. Sample 73119PK4 is a weakly deformed, biotite-rich granitoid dike from the same outcrop that crosscuts the host mylonite fabrics (Fig. 5C). The shear zone foliation at this locality dips steeply to the SW (162, 68), and the mineral lineation plunges shallowly to the SE (157, 17).

Sample 8219PK2 is a mylonitized, coarse-grained, biotite-hornblende granitoid sill from an island off the southern tip of Don Peninsula (Fig. 4). The foliation is defined by euhedral plagioclase lathes, books of biotite, prolate quartz ribbons, and minor euhedral K-feldspar. Plagioclase grains in thin section display albite twins oriented parallel to the subhorizontal stretching lineation, suggesting deformation occurred in the magmatic state before later brittle-ductile overprinting during solid-state mylonitization (Fig. 7B; Paterson et al., 1989). Sample 8219PK1 is a fine-grained, K-feldspar–rich leucocratic dike from the same outcrop that crosscuts the local mylonitic foliation. The dike is foliated subparallel to the local host-rock fabric, but the margins of the dike are undeformed. The shear zone foliation at this locality dips moderately to the SE (033, 52), while the mineral lineation rake varies significantly, ranging from subhorizontal to downdip. Steeply plunging mineral lineations in a transpressional setting indicate a higher pure-to-simple shear ratio and vertical stretching (Tikoff and Greene, 1997; Lin et al., 1998), which may correspond to a left-stepping restraining bend in the shear zone trace at these latitudes.

METHODS

Large-*n* LA-ICP-MS Geochronology

All samples were analyzed using standard methods of zircon U-Pb LA-ICP-MS geochronology at the Arizona LaserChron Center (ALC; www.laserchron.org; Gehrels et al., 2008; Gehrels and Pecha, 2014), and large-*n* methods were applied (Sundell et al., 2021) in an effort to improve precision and accuracy of measurements. One sample (73119PK1) was not analyzed using large-*n* methods due to low zircon yield (<30) and variable U content and was instead analyzed following the lower-*n* methods of Gehrels and Pecha (2014).

Zircon Separation, Mount Preparation, and Data Acquisition

Zircons were separated from ~2 kg samples using traditional methods of crushing, pulverizing, water separation, magnetic separation, and heavy liquids separation at the ALC (Gehrels et al., 2008). Between 30 and 50 grains were picked and mounted in epoxy with FC-1 (isotope dilution–thermal ionization mass spectrometry [ID-TIMS] age of 1099.0 ± 0.6 Ma) as a primary reference material (RM) and GHR1 (ID-TIMS age of 48.106 ± 0.023 Ma), SL-F (ID-TIMS age of 555.86 ± 0.68 Ma), R33 (ID-TIMS age of 419.3 ± 0.4 Ma), and TEM (ID-TIMS age of 416.78 ± 0.33 Ma) as secondary RMs (Paces and Miller, 1993; Black et al., 2004; S. Bowring, 2017, personal commun. with George Gehrels regarding unpublished report titled "MIT LA SRI LAN F" that details the ID-TIMS age for a

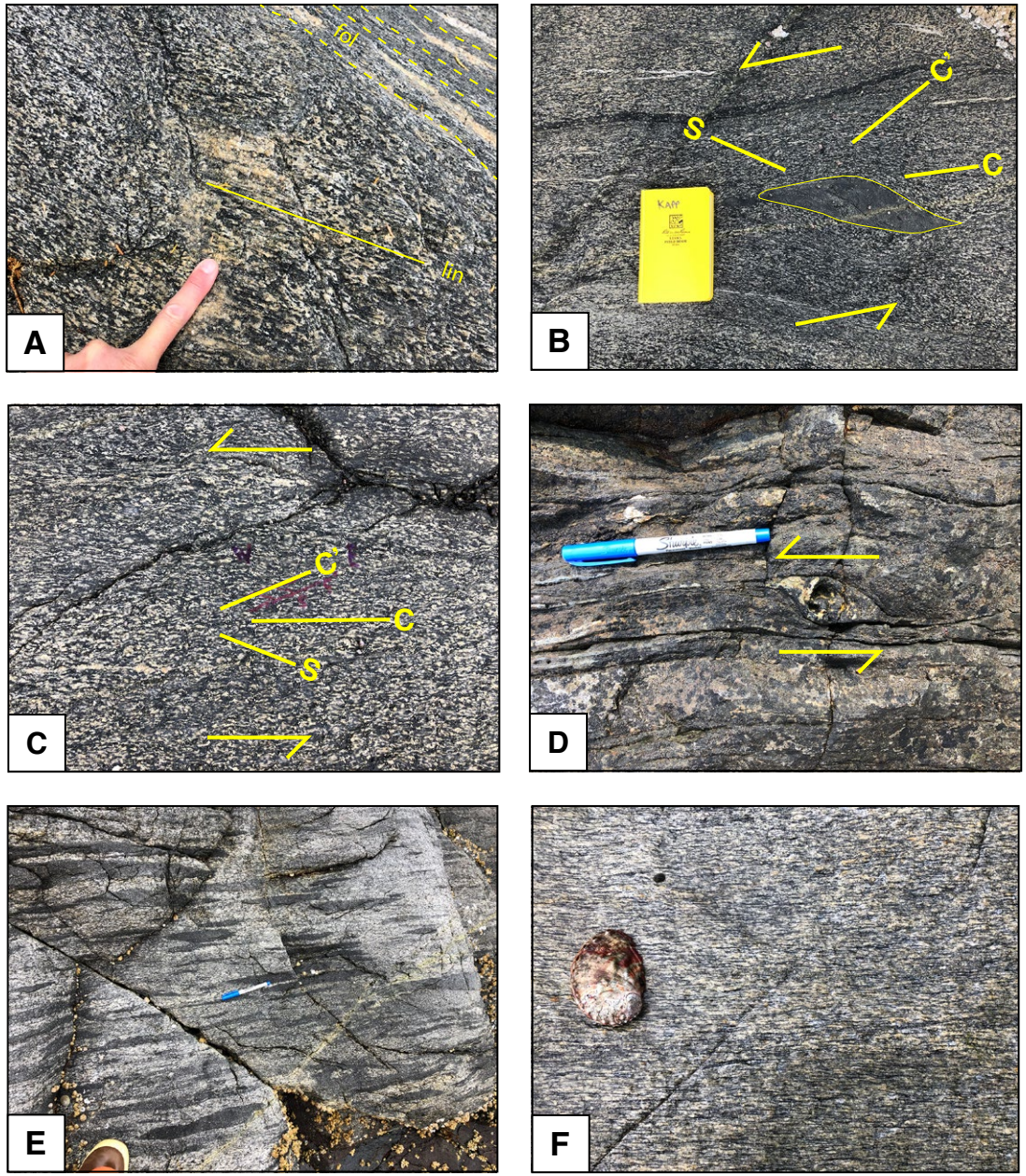

Figure 6. Outcrop photos of structural fabrics in the Kitkatla and Grenville Channel shear zones. (A) Subvertical foliation (fol) and subhorizontal lineation (lin) in Kitkatla shear zone (53°34′13.15″N, 129°59′12.919″W). (B) Mafic enclaves flattened and stretched parallel to S plane in S-C-C′ mylonite showing sinistral sense of shear (same location as A). (C) Close-up view of S-C-C′ fabrics at the same outcrop as A and B, showing penetrative sinistral sense of shear. Pen length is 14 cm. (D) Partially eroded σ-clast in the Kitkatla shear zone showing sinistral sense of shear (53°20′9.16″N, 129°20′25.139″W). (E) Flattened mafic enclaves in tonalite near Klemtu (52°40′27.209″N, 128°32′44.41″W). (F) Ultramylonite near Klemtu with finely spaced S-C fabrics (52°33′58.759″N, 128°30′35.71″W). Hammer length is 122 cm.

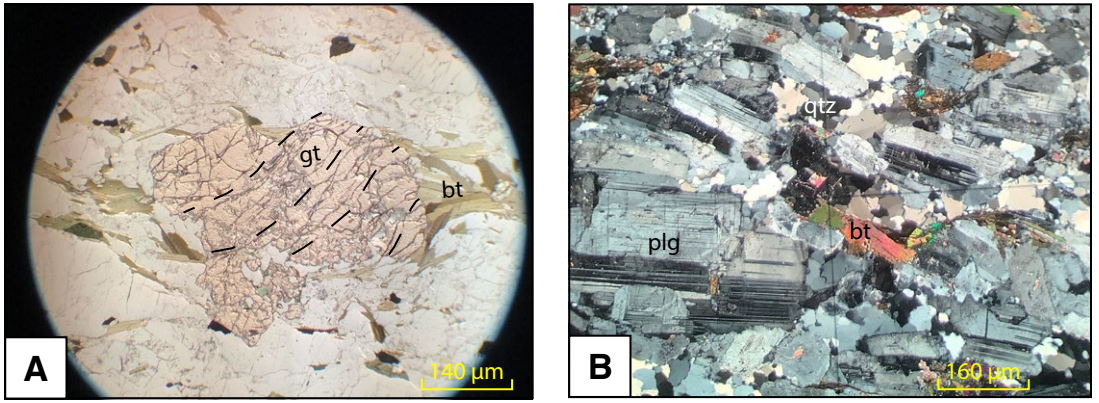

Figure 7. Photomicrographs showing microstructural fabrics in shear zone samples. (A) Rotated garnet porphyroclast from southern Grenville Channel with biotite delta tails (plane-polarized light). (B) Magmatic-state fabric defined by aligned plagioclase lathes with albite twins weakly overprinted by solid-state protomylonitic deformation (cross-polarized light). Abbreviations: gt—garnet; bt—biotite; plg—plagioclase feldspar; qtz—quartz.

primary reference material; Eddy et al., 2019). Backscattered electron (BSE) and cathodoluminescence (CL) images of grain mounts were produced on a Hitachi 3400N scanning electron microscope (SEM) with a Gatan Chroma CL system to identify and target distinct textural domains in sample grains prior to data acquisition (Fig. 8). Each of the grains analyzed and the locations of the analysis spots are shown in the tables and figures of the Supplemental Material.[1] Large-*n* igneous zircon U-Pb analysis was conducted by LA-ICP-MS at the ALC following the rapid "time-resolved" method of Sundell et al. (2021).

Instrumentation consisted of a Photon Machines Analyte-G2 ArF 193 nm excimer laser with a HelEx2 sample cell connected to a Nu Instruments high-resolution multicollector ICP-MS via an aerosol rapid introduction system (ARIS) (Table 1). In total, 100 unknowns, ~210 primary RMs (FC-1), and 25 of each secondary RM were analyzed during each session to evaluate any systematic shifts in age dispersion and accuracy based on offset from known ID-TIMS ages (Fig. 8; see Data Reduction, Interpretation, and Error Propagation section). Prior to the first analysis, all laser spots were targeted and slightly ablated with a 50 µm cleaning shot to remove common Pb and/or other surface contaminants. A spot size of 30 µm was used during each analysis to ablate to a depth of ~15 µm. Ablated material was carried by helium gas into the plasma source of the mass spectrometer and measured using Faraday detectors at a rate of 300 analyses/h in time-resolved analysis mode with a 0.2 s resolution (Sundell et al., 2021).

One sample (73119PK1) yielded zircons with highly variable U content that would sometimes exceed detector limits, making the automated large-*n* routine of Sundell et al. (2021) untenable. Zircons from 73119PK1 were instead analyzed in isotope analysis mode following the methods of Gehrels and Pecha (2014) using the same instrumentation and analytical methods as above (Table 1).

Data Reduction, Interpretation, and Error Propagation

All isotopic data were first processed off-line using the MATLAB program AgeCalcML (github.com/kurtsundell/AgeCalcML; Sundell et al., 2021), which automatically produces workable data sheets that conform to the data-reporting protocols of Horstwood et al. (2016) (Table 2). In this first phase of data reduction, individual analyses that yielded high ^{204}Pb (>600 cps [counts per second]), high $^{206}Pb/^{238}U$ uncertainty (>10% at 1σ), high reverse discordance (>5% at 1σ), and/or high discordance (>20%) were removed from further consideration.

Uncertainties associated with U/Pb fractionation corrections at the ALC are typically propagated through for systematic uncertainty by taking the standard error of the mean of ~10 of the closest primary RMs within the sample-standard bracketing (Gehrels et al., 2008; Gehrels and Pecha, 2014). Unique to this study, the propagation of fractionation uncertainties into the systematic uncertainty was achieved by taking the standard error of the mean of all analyses of the primary RM in a session. This whole-session averaging is tenable only when instrument drift is low, which is often true at the ALC (see Table S2 for analysis of primary RM behavior by individual sample session, footnote 1). The secondary RMs also did not show systematic offsets from accepted ID-TIMS ages and produced an average mean squared weighted deviation (MSWD) of ~1 within individual sessions (Fig. 9), validating the approach.

All analyzed samples had distinct core domains that may represent inherited material from the source rock host (xenocrysts), early crystallization during protracted cooling of the magma (antecrysts),

[1]Supplemental Material. Table S1: U-Pb geochronologic analyses of unknowns. Table S2: U-Pb geochronologic analyses of primary reference materials. Table S3: U-Pb geochronologic analyses of secondary reference materials. Table S4: U-Pb geochronologic analyses of secondary reference materials from 11 different instrument-validation sessions conducted from 2019 to 2021. Please visit https://doi.org/10.1130/GEOS.S.21357489 to access the supplemental material, and contact editing@geosociety.org with any questions.

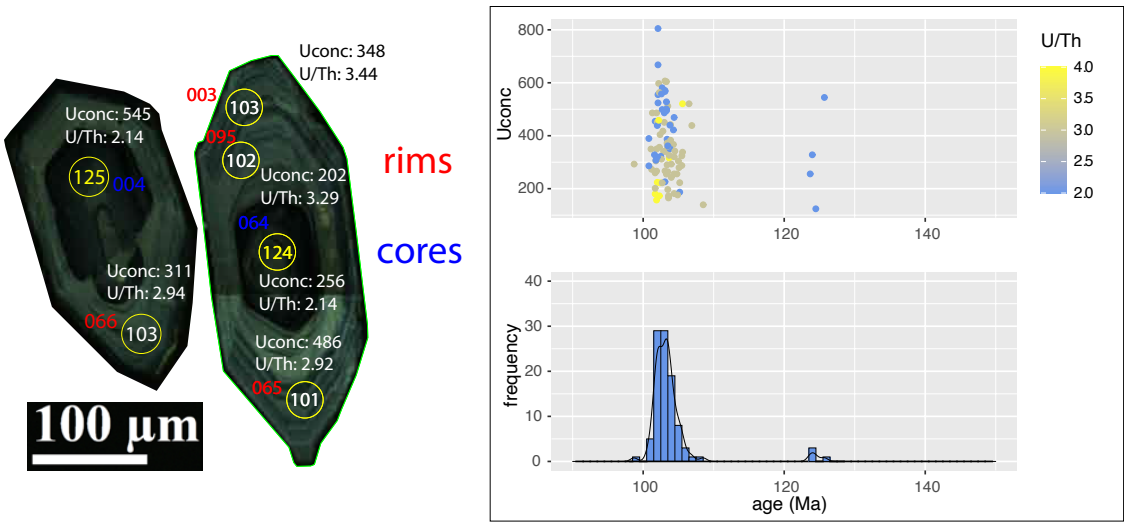

Figure 8. (Left) Annotated cathodoluminescence images of zircon grains for sample 73119PK2 showing locations of 30 µm spot analyses overlayed with $^{206}Pb/^{238}U$ age, U concentration, and U/Th ratio. Note the general homogeneity of zircon textures except for the darker cores, which yielded older Early Cretaceous ages. (Right) Plots of U concentration vs. age showing U/Th ratio by color (top) and age histogram overlain by probability density profile (bottom). Note older age mode of 125–124 Ma xenocrysts.

or late crystallization during the final formation of the rock (autocrysts), as well as younger rims. To aid in interpretation, analysis spots were shown on CL images and categorized as rims, cores, or mixed analyses (R, C, and M, respectively, in the Supplemental Material files). The resulting core ages were then interpreted within the context of U-Pb ages and chemical compositions (Uconc and U/Th ratios) as xenocrysts, antecrysts, or autocrysts. Crystallization ages for the rocks were based on weighted averages of analyses from rim domains only, as they represent the youngest magmatic addition of new zircon. Results from analyses that overlapped multiple domains were labeled as mixed analyses and not used for age interpretations. All weighted averages were calculated using IsoPlotR (Vermeesch, 2018).

After a weighted average of rim analyses had been calculated for a sample, we used the MSWD of the data set as a tool for evaluating whether the age represented a true crystallization age with a unimodal Gaussian distribution. If the uncertainties appropriately represented the dispersion of data ("normal dispersion"; i.e., MSWD ~1; Wendt and Carl, 1991), then the modified Chauvenet outlier-rejection criteria of IsoPlotR were applied, and the weighted mean age was reported as the crystallization age, unless geologic (textural, chemical) evidence suggested otherwise. Fortunately, all but three of our samples exhibited normal dispersion, resulting in simple age interpretations.

For one sample (73119PK4), the weighted average of rim analyses yielded an MSWD of 4.4, and the probability density profile of the analyses was non-Gaussian with two distinct but overlapping modes, indicating a potential geologic source for overdispersion. We evaluated potential sources of overdispersion by examining plots of U concentration versus age, U/Th versus age, age probability

TABLE 1. PARAMETERS FOR LASER AND MASS SPECTROMETER IN LARGE-*n* IGNEOUS ZIRCON U-Pb METHOD

Parameter	Instrumentation
Laser	
Type and wavelength	Photon Analyte-G2 193 nm excimer laser
Sample cell	HelEx
Constant energy set	7 mJ
Laser energy	100% (open gate)
Repetition rate	7 Hz
MFC1, MFC2 He	0.10, 0.30 L min^{-1}
Pre-ablation pass	Three bursts at 50 µm
Laser beam diameter	30 µm
Mass spectrometer	
Type	Nu Instruments high-resolution multicollector
Cool gas	13.0 L min^{-1}
Auxiliary gas	0.80 L min^{-1}
Sample/make-up gas	1.06 L min^{-1}
Radio frequency power	1300 W
Masses measured (Faraday)	^{206}Pb, ^{207}Pb, ^{208}Pb, ^{232}Th, ^{238}U
Collector configuration—mass (Faraday)	ExH-238, H2-232, L6-208, L7-207, L8-206

TABLE 2. EXAMPLE U-Pb DATA TABLE FOR SAMPLE 73119PK2, WITH ANALYSES SORTED BY TEXTURAL ZONE AND $^{206}Pb/^{238}U$ AGE

Analysis/zircon	Zone	U (ppm)	Th (ppm)	U/Th	Corrected isotopic ratios								Rho	% disc.*	Corrected ages (Ma)						Best age ± (Ma)
					$^{206}Pb/^{207}Pb$	Err %	$^{207}Pb/^{235}U$	Err %	$^{206}Pb/^{238}U$	Err %	$^{208}Pb/^{232}Th$	Err %			$^{206}Pb/^{238}U$	±2s	$^{207}Pb/^{235}U$	±2s	$^{207}Pb/^{206}Pb$	±2s	
Sample 73119PK2, Northern Klemtu mylonitized host rock (Klemtu, British Columbia), January 2020																					
73119PK2 90	R	293	99	3	11.11297	8.3	0.19134	8.4	0.01543	1.2	0.00496	8.5	0.137	44	98.7	1.1	177.8	13.7	1425.2	158.9	98.7 ± 1.128
73119PK2 99	R	390	168	2	12.82712	7.1	0.16926	7.2	0.01575	1.2	0.00509	7.1	0.170	37	100.8	1.2	158.8	10.6	1145.9	141.3	100.8 ± 1.226
73119PK2 62	R	286	125	2	10.87926	11.0	0.19970	11.0	0.01576	1.2	0.00489	7.9	0.111	45	100.8	1.2	184.9	18.6	1465.7	208.8	100.8 ± 1.228
73119PK2 82	R	350	128	3	12.63300	6.9	0.17237	7.0	0.01580	1.2	0.00480	6.4	0.177	37	101.1	1.2	161.5	10.4	1176.1	136.0	101.1 ± 1.237
73119PK2 50	R	273	93	3	11.47676	10.7	0.18999	10.9	0.01582	1.9	0.00479	10.6	0.176	43	101.2	1.9	176.6	17.7	1363.4	207.3	101.2 ± 1.924
73119PK2 65	R	486	167	3	14.49010	6.7	0.15062	6.7	0.01584	0.9	0.00468	7.5	0.128	29	101.3	0.9	142.5	9.0	899.1	137.9	101.3 ± 0.866
73119PK2 71	R	328	135	2	11.27406	9.8	0.19424	9.9	0.01589	1.2	0.00489	8.8	0.126	44	101.6	1.3	180.2	16.4	1397.7	189.2	101.6 ± 1.26
73119PK2 24	R	455	193	2	13.23817	7.3	0.16548	7.3	0.01590	1.0	0.00439	5.5	0.135	35	101.7	1.0	155.5	10.5	1082.9	145.6	101.7 ± 0.996
73119PK2 92	R	180	43	4	8.97741	9.1	0.24411	9.2	0.01590	1.6	0.00524	15.3	0.174	54	101.7	1.6	221.8	18.4	1822.2	165.6	101.7 ± 1.62
73119PK2 51	R	260	95	3	9.37822	9.3	0.23368	9.4	0.01590	1.2	0.00450	10.4	0.127	52	101.7	1.2	213.2	18.1	1742.6	171.1	101.7 ± 1.205
73119PK2 95	R	202	61	3	9.04480	12.8	0.24233	12.9	0.01590	1.4	0.00419	15.9	0.105	54	101.7	1.4	220.3	25.6	1808.6	234.2	101.7 ± 1.372
73119PK2 83	R	305	97	3	10.66732	8.5	0.20555	8.6	0.01591	1.2	0.00472	10.9	0.135	46	101.8	1.2	189.8	14.8	1503.0	160.8	101.8 ± 1.17
73119PK2 87	R	307	132	2	12.91289	8.3	0.16985	8.4	0.01591	1.1	0.00500	8.3	0.137	36	101.8	1.2	159.3	12.3	1132.6	165.1	101.8 ± 1.153
73119PK2 9	R	311	114	3	11.80936	9.3	0.18585	9.4	0.01593	1.2	0.00489	8.3	0.126	41	101.9	1.2	173.1	14.9	1308.2	180.6	101.9 ± 1.188
73119PK2 21	R	266	98	3	10.81031	11.5	0.20313	11.5	0.01593	0.9	0.00433	9.6	0.081	46	101.9	0.9	187.8	19.8	1477.7	218.6	101.9 ± 0.938
73119PK2 31	R	350	105	3	12.34308	9.6	0.17791	9.6	0.01593	0.9	0.00574	8.5	0.097	39	101.9	0.9	166.3	14.7	1221.8	188.4	101.9 ± 0.942
73119PK2 33	R	486	191	3	16.38677	5.9	0.13403	6.0	0.01594	1.1	0.00487	6.0	0.175	20	101.9	1.1	127.7	7.2	640.1	127.0	101.9 ± 1.063
73119PK2 72	R	157	37	4	9.07586	11.9	0.24200	11.9	0.01594	1.4	0.00675	18.2	0.118	54	101.9	1.4	220.1	23.6	1802.4	216.4	101.9 ± 1.422
73119PK2 91	R	319	132	2	12.45621	8.0	0.17641	8.0	0.01594	1.2	0.00501	6.5	0.143	38	102.0	1.2	165.0	12.2	1203.9	157.0	102.0 ± 1.165
73119PK2 63	R	224	58	4	12.26378	12.9	0.17919	12.9	0.01595	1.3	0.00534	15.5	0.098	39	102.0	1.3	167.4	19.9	1234.5	253.2	102.0 ± 1.282
73119PK2 67	R	439	210	2	13.26396	8.5	0.16572	8.7	0.01595	1.6	0.00581	6.4	0.181	34	102.0	1.6	155.7	12.5	1079.0	171.5	102.0 ± 1.592
73119PK2 34	R	452	179	3	14.00522	7.6	0.15695	7.7	0.01595	1.2	0.00472	6.9	0.158	31	102.0	1.2	148.0	10.6	968.9	155.0	102.0 ± 1.226
73119PK2 59	R	668	279	2	15.15056	4.8	0.14516	4.9	0.01596	0.9	0.00472	4.5	0.174	26	102.1	0.9	137.6	6.3	806.5	101.0	102.1 ± 0.865
73119PK2 20	R	555	243	2	15.61218	6.8	0.14091	6.9	0.01596	0.8	0.00488	4.7	0.109	24	102.1	0.8	133.9	8.6	743.3	144.4	102.1 ± 0.76
73119PK2 86	R	524	243	2	16.27860	4.8	0.13515	4.9	0.01596	0.9	0.00487	5.3	0.181	21	102.1	0.9	128.7	5.9	654.3	102.9	102.1 ± 0.894
73119PK2 40	R	805	474	2	17.57117	3.9	0.12525	3.9	0.01597	0.8	0.00505	3.4	0.198	15	102.1	0.8	119.8	4.4	488.1	85.2	102.1 ± 0.789
73119PK2 88	R	459	128	4	13.26762	6.7	0.16593	6.8	0.01597	1.0	0.00483	8.8	0.141	34	102.2	1.0	155.9	9.8	1078.4	134.5	102.2 ± 0.966
73119PK2 1	R	598	184	3	13.91386	6.2	0.15832	6.2	0.01598	0.9	0.00514	6.6	0.143	32	102.2	0.9	149.2	8.6	982.3	125.6	102.2 ± 0.904
73119PK2 11	R	453	184	2	13.73326	7.8	0.16043	7.9	0.01599	1.1	0.00458	5.4	0.139	32	102.2	1.1	151.1	11.0	1008.8	158.2	102.2 ± 1.108
73119PK2 78	R	356	114	3	12.58621	7.5	0.17507	7.5	0.01599	0.9	0.00433	9.6	0.125	38	102.3	1.0	163.8	11.4	1183.4	147.8	102.3 ± 0.952
73119PK2 57	R	563	195	3	15.27722	5.4	0.14428	5.5	0.01599	0.9	0.00474	5.6	0.165	25	102.3	0.9	136.8	7.0	789.0	112.9	102.3 ± 0.914
73119PK2 58	R	173	45	4	7.65654	13.7	0.28802	13.9	0.01600	2.2	0.00603	18.1	0.156	60	102.3	2.2	257.0	31.6	2106.1	242.1	102.3 ± 2.196
73119PK2 61	R	222	63	4	10.44453	11.9	0.21122	12.2	0.01601	2.5	0.00487	13.0	0.205	47	102.4	2.5	194.6	21.5	1542.7	224.5	102.4 ± 2.532
73119PK2 30	R	404	131	3	13.75985	6.1	0.16040	6.2	0.01601	1.0	0.00494	7.8	0.164	32	102.4	1.0	151.1	8.7	1004.9	124.5	102.4 ± 1.038
73119PK2 54	R	322	140	2	13.21067	9.1	0.16721	9.3	0.01603	1.9	0.00451	6.9	0.207	35	102.5	2.0	157.0	13.5	1087.1	182.9	102.5 ± 1.96
73119PK2 66	R	311	106	3	11.10294	8.6	0.19906	8.8	0.01604	1.6	0.00505	9.4	0.178	44	102.6	1.6	184.3	14.8	1426.9	164.8	102.6 ± 1.588
73119PK2 98	R	558	250	2	13.80808	5.7	0.16011	5.7	0.01604	0.8	0.00495	4.8	0.139	32	102.6	0.8	150.8	8.0	997.8	115.6	102.6 ± 0.815
73119PK2 41	R	499	210	2	14.16003	5.2	0.15625	5.3	0.01605	0.8	0.00494	4.9	0.161	30	102.7	0.9	147.4	7.3	946.5	106.9	102.7 ± 0.866
73119PK2 94	R	222	80	3	9.79595	11.4	0.22591	11.4	0.01606	1.1	0.00477	12.6	0.100	50	102.7	1.2	206.8	21.4	1662.3	211.5	102.7 ± 1.171
73119PK2 28	R	581	236	2	15.18613	5.6	0.14574	5.6	0.01606	0.9	0.00505	5.1	0.158	26	102.7	0.9	138.1	7.3	801.6	116.8	102.7 ± 0.911
73119PK2 15	R	417	125	3	12.49809	8.3	0.17725	8.3	0.01607	0.9	0.00478	8.7	0.111	38	102.8	0.9	165.7	12.7	1197.3	163.0	102.8 ± 0.936
73119PK2 35	R	341	133	3	13.08761	9.1	0.16945	9.2	0.01609	0.8	0.00475	6.2	0.089	35	102.9	0.8	158.9	13.5	1105.8	182.5	102.9 ± 0.829
73119PK2 23	R	451	165	3	13.40404	6.7	0.16554	6.9	0.01610	1.7	0.00489	5.7	0.250	34	103.0	1.8	155.5	10.0	1057.9	135.5	103.0 ± 1.772
73119PK2 13	R	486	225	2	13.69172	8.5	0.16211	8.5	0.01610	0.9	0.00498	8.2	0.106	32	103.0	0.9	152.5	12.1	1015.0	172.1	103.0 ± 0.925
73119PK2 32	R	567	234	2	15.68753	4.8	0.14158	4.9	0.01612	0.8	0.00486	4.5	0.160	23	103.1	0.8	134.5	6.2	733.2	102.8	103.1 ± 0.805
73119PK2 42	R	267	84	3	11.55828	9.7	0.19219	9.8	0.01612	1.7	0.00473	12.4	0.176	42	103.1	1.8	178.5	16.1	1349.8	186.8	103.1 ± 1.769
73119PK2 75	R	607	236	3	13.44523	7.1	0.16525	7.1	0.01612	0.8	0.00477	5.2	0.113	34	103.1	0.8	155.3	10.2	1051.7	142.3	103.1 ± 0.821
73119PK2 8	R	571	229	2	16.00762	4.9	0.13882	5.0	0.01612	0.8	0.00534	4.0	0.156	22	103.1	0.8	132.0	6.2	690.2	105.0	103.1 ± 0.795
73119PK2 73	R	226	100	2	11.86596	9.6	0.18727	9.7	0.01612	1.3	0.00487	10.7	0.137	41	103.1	1.4	174.3	15.6	1298.9	187.7	103.1 ± 1.363
73119PK2 53	R	341	112	3	14.96201	5.6	0.14860	5.7	0.01613	1.2	0.00496	8.9	0.206	27	103.2	1.2	140.7	7.5	832.6	116.9	103.2 ± 1.207

(*continued*)

TABLE 2. EXAMPLE U-Pb DATA TABLE FOR SAMPLE 73119PK2, WITH ANALYSES SORTED BY TEXTURAL ZONE AND $^{206}Pb/^{238}U$ AGE (*continued*)

Analysis/zircon	Zone	U (ppm)	Th (ppm)	U/Th	Corrected isotopic ratios								Rho	% disc.*	Corrected ages (Ma)						Best age ± (Ma)
					$^{206}Pb/^{207}Pb$	Err %	$^{207}Pb/^{235}U$	Err %	$^{206}Pb/^{238}U$	Err %	$^{208}Pb/^{232}Th$	Err %			$^{206}Pb/^{238}U$	±2s	$^{207}Pb/^{235}U$	±2s	$^{207}Pb/^{206}Pb$	±2s	
73119PK2 10	R	494	241	2	15.68681	6.4	0.14187	6.4	0.01615	0.8	0.00491	5.0	0.123	23	103.3	0.8	134.7	8.1	733.3	135.4	103.3 ± 0.81
73119PK2 44	R	501	211	2	14.82747	7.8	0.15010	7.8	0.01615	1.0	0.00514	5.4	0.133	27	103.3	1.1	142.0	10.4	851.5	161.3	103.3 ± 1.065
73119PK2 18	R	528	221	2	14.90100	5.3	0.14941	5.5	0.01615	1.4	0.00500	4.9	0.247	27	103.3	1.4	141.4	7.3	841.2	111.4	103.3 ± 1.398
73119PK2 97	R	255	79	3	9.80688	12.0	0.22705	12.1	0.01616	1.4	0.00453	12.5	0.116	50	103.3	1.4	207.8	22.7	1660.3	222.5	103.3 ± 1.433
73119PK2 45	R	604	206	3	16.85306	5.6	0.13214	5.7	0.01616	0.8	0.00517	7.6	0.143	18	103.3	0.8	126.0	6.7	579.5	122.5	103.3 ± 0.836
73119PK2 27	R	387	188	2	12.47110	8.9	0.17864	9.0	0.01616	1.2	0.00461	6.0	0.135	38	103.4	1.3	166.9	13.9	1201.6	176.3	103.4 ± 1.251
73119PK2 3	R	348	101	3	11.83307	8.5	0.18837	8.6	0.01617	1.2	0.00546	7.3	0.141	41	103.4	1.2	175.2	13.8	1304.3	164.8	103.4 ± 1.235
73119PK2 19	R	290	97	3	11.44820	10.9	0.19473	11.0	0.01618	1.2	0.00455	10.6	0.107	43	103.4	1.2	180.7	18.2	1368.2	211.3	103.4 ± 1.206
73119PK2 69	R	372	124	3	12.41994	8.3	0.17951	8.4	0.01618	1.3	0.00481	10.6	0.150	38	103.4	1.3	167.6	13.0	1209.7	164.5	103.4 ± 1.299
73119PK2 2	R	512	176	3	13.83458	5.6	0.16116	5.7	0.01618	0.9	0.00535	6.4	0.158	32	103.5	0.9	151.7	8.0	993.9	114.5	103.5 ± 0.926
73119PK2 84	R	197	57	3	9.63592	10.2	0.23141	10.3	0.01618	1.3	0.00499	10.5	0.127	51	103.5	1.3	211.4	19.6	1692.7	188.2	103.5 ± 1.336
73119PK2 93	R	362	161	2	11.58491	9.2	0.19251	9.3	0.01618	1.1	0.00442	8.2	0.124	42	103.5	1.2	178.8	15.2	1345.3	177.6	103.5 ± 1.173
73119PK2 89	R	360	115	3	11.50326	5.6	0.19398	5.7	0.01619	0.9	0.00539	9.4	0.165	42	103.5	1.0	180.0	9.3	1359.0	107.7	103.5 ± 0.962
73119PK2 60	R	264	80	3	10.99063	9.5	0.20305	9.6	0.01619	1.2	0.00479	12.6	0.128	45	103.5	1.3	187.7	16.5	1446.3	182.0	103.5 ± 1.263
73119PK2 6	R	357	115	3	12.78741	7.2	0.17458	7.2	0.01620	0.9	0.00514	7.6	0.118	37	103.6	0.9	163.4	10.9	1152.0	142.8	103.6 ± 0.877
73119PK2 96	R	165	52	3	7.55856	16.0	0.29546	16.1	0.01620	1.8	0.00538	16.3	0.110	61	103.6	1.8	262.8	37.3	2128.7	282.3	103.6 ± 1.827
73119PK2 74	R	173	64	3	8.04317	10.6	0.27765	10.7	0.01620	1.7	0.00518	15.0	0.157	58	103.6	1.7	248.8	23.7	2019.2	188.2	103.6 ± 1.729
73119PK2 37	R	326	93	3	12.85739	8.3	0.17387	8.4	0.01622	1.2	0.00477	12.2	0.143	36	103.7	1.2	162.8	12.6	1141.1	165.0	103.7 ± 1.233
73119PK2 29	R	316	87	4	10.50279	9.7	0.21290	9.8	0.01622	1.1	0.00447	13.2	0.116	47	103.7	1.2	196.0	17.4	1532.3	183.0	103.7 ± 1.17
73119PK2 52	R	440	185	2	13.12208	7.3	0.17048	7.4	0.01623	1.1	0.00497	7.4	0.148	35	103.8	1.1	159.8	10.9	1100.5	146.5	103.8 ± 1.127
73119PK2 80	R	351	142	2	13.01320	8.0	0.17193	8.1	0.01623	1.2	0.00466	8.0	0.151	36	103.8	1.3	161.1	12.1	1117.2	160.6	103.8 ± 1.268
73119PK2 70	R	383	153	3	12.50225	8.2	0.17909	8.2	0.01625	0.9	0.00471	8.4	0.110	38	103.9	0.9	167.3	12.7	1196.6	161.7	103.9 ± 0.932
73119PK2 39	R	373	145	3	12.77063	6.8	0.17537	6.9	0.01625	1.0	0.00480	6.3	0.145	37	103.9	1.0	164.1	10.4	1154.6	135.3	103.9 ± 1.028
73119PK2 7	R	442	147	3	14.85614	7.7	0.15079	7.8	0.01625	1.1	0.00482	8.4	0.141	27	103.9	1.1	142.6	10.4	847.5	160.6	103.9 ± 1.131
73119PK2 22	R	243	77	3	10.08470	10.2	0.22228	10.3	0.01627	1.1	0.00496	10.2	0.112	49	104.0	1.2	203.8	18.9	1608.4	190.4	104.0 ± 1.184
73119PK2 43	R	293	113	3	11.42928	10.2	0.19615	10.4	0.01627	2.0	0.00486	7.4	0.193	43	104.0	2.1	181.9	17.3	1371.4	196.6	104.0 ± 2.068
73119PK2 38	R	422	175	2	13.71022	6.6	0.16397	6.7	0.01631	1.1	0.00456	6.3	0.162	32	104.3	1.1	154.2	9.6	1012.2	134.3	104.3 ± 1.121
73119PK2 56	R	367	143	3	12.87448	8.9	0.17466	9.0	0.01632	1.2	0.00502	8.7	0.137	36	104.3	1.3	163.5	13.6	1138.5	177.2	104.3 ± 1.27
73119PK2 85	R	321	98	3	9.58369	8.4	0.23473	8.5	0.01632	1.1	0.00454	8.5	0.128	51	104.4	1.1	214.1	16.4	1702.8	155.3	104.4 ± 1.124
73119PK2 5	R	469	211	2	15.07963	6.6	0.14922	6.7	0.01633	0.9	0.00506	7.1	0.135	26	104.4	0.9	141.2	8.8	816.3	137.9	104.4 ± 0.926
73119PK2 25	R	256	97	3	12.63447	9.1	0.17811	9.2	0.01633	1.3	0.00378	11.1	0.143	37	104.4	1.4	166.4	14.1	1175.9	180.1	104.4 ± 1.356
73119PK2 26	R	182	58	3	8.85045	13.1	0.25434	13.3	0.01633	1.7	0.00439	15.3	0.125	55	104.4	1.7	230.1	27.3	1848.0	238.9	104.4 ± 1.711
73119PK2 81	R	342	135	3	13.33977	7.1	0.16880	7.2	0.01634	1.0	0.00561	7.3	0.143	34	104.5	1.1	158.4	10.6	1067.6	143.8	104.5 ± 1.069
73119PK2 14	R	256	94	3	11.36202	10.0	0.19890	10.1	0.01640	1.4	0.00414	10.4	0.135	43	104.8	1.4	184.2	17.0	1382.7	192.3	104.8 ± 1.412
73119PK2 76	R	176	53	3	8.64917	12.6	0.26131	12.7	0.01640	1.8	0.00456	14.0	0.140	56	104.9	1.9	235.7	26.8	1889.5	227.7	104.9 ± 1.85
73119PK2 100	R	305	94	3	11.28363	10.6	0.20054	10.7	0.01642	1.3	0.00506	12.2	0.124	43	105.0	1.4	185.6	18.1	1396.0	203.5	105.0 ± 1.375
73119PK2 49	R	280	92	3	10.84939	7.0	0.20875	7.1	0.01643	1.3	0.00465	10.6	0.188	45	105.1	1.4	192.5	12.5	1470.9	133.3	105.1 ± 1.397
73119PK2 36	R	223	75	3	10.16881	12.5	0.22294	12.6	0.01645	1.4	0.00412	13.1	0.108	49	105.2	1.4	204.4	23.3	1592.9	234.4	105.2 ± 1.419
73119PK2 68	R	187	81	2	8.98492	10.1	0.25233	10.3	0.01645	1.7	0.00421	11.8	0.163	54	105.2	1.7	228.5	21.0	1820.7	184.2	105.2 ± 1.741
73119PK2 16	R	324	120	3	13.78982	7.4	0.16487	7.5	0.01650	1.5	0.00496	7.2	0.195	32	105.5	1.5	155.0	10.8	1000.5	150.0	105.5 ± 1.537
73119PK2 79	R	288	94	3	13.46365	7.4	0.16894	7.5	0.01650	1.1	0.00499	10.9	0.147	33	105.5	1.2	158.5	11.1	1048.9	150.4	105.5 ± 1.163
73119PK2 77	R	338	111	3	14.77223	7.8	0.15403	7.9	0.01651	1.2	0.00538	9.8	0.151	27	105.6	1.2	145.5	10.7	859.2	161.9	105.6 ± 1.249
73119PK2 17	R	521	147	4	15.52105	5.3	0.14672	5.4	0.01652	1.0	0.00484	6.4	0.194	24	105.6	1.1	139.0	7.0	755.7	111.4	105.6 ± 1.093
73119PK2 46	R	521	200	3	14.46741	6.1	0.15862	6.2	0.01665	1.0	0.00496	6.0	0.154	29	106.5	1.0	149.5	8.6	902.3	126.8	106.5 ± 1.014
73119PK2 12	R	439	165	3	13.33831	5.2	0.17278	5.3	0.01672	0.9	0.00541	5.9	0.174	34	106.9	1.0	161.8	7.9	1067.8	104.2	106.9 ± 0.97
73119PK2 55	R	139	53	3	5.92324	14.0	0.39494	14.1	0.01697	1.7	0.00480	16.2	0.123	68	108.5	1.9	338.0	40.4	2546.0	235.0	108.5 ± 1.859
73119PK2 64	C	256	119	2	11.01543	11.4	0.24249	11.5	0.01938	1.1	0.00578	7.9	0.099	44	123.7	1.4	220.5	22.8	1442.0	218.9	123.7 ± 1.391
73119PK2 48	C	328	142	2	13.84401	10.2	0.19334	10.2	0.01942	0.9	0.00549	6.8	0.087	31	124.0	1.1	179.5	16.8	992.5	207.8	124.0 ± 1.095
73119PK2 47	C	124	54	2	8.47126	12.6	0.31729	12.8	0.01950	2.0	0.00548	13.4	0.154	56	124.5	2.4	279.8	31.3	1926.8	227.6	124.5 ± 2.433
73119PK2 4	C	545	255	2	16.98240	4.5	0.15975	4.6	0.01968	0.8	0.00636	4.0	0.168	16	125.7	1.0	150.5	6.4	562.8	98.4	125.7 ± 0.958

*disc.—discordance.

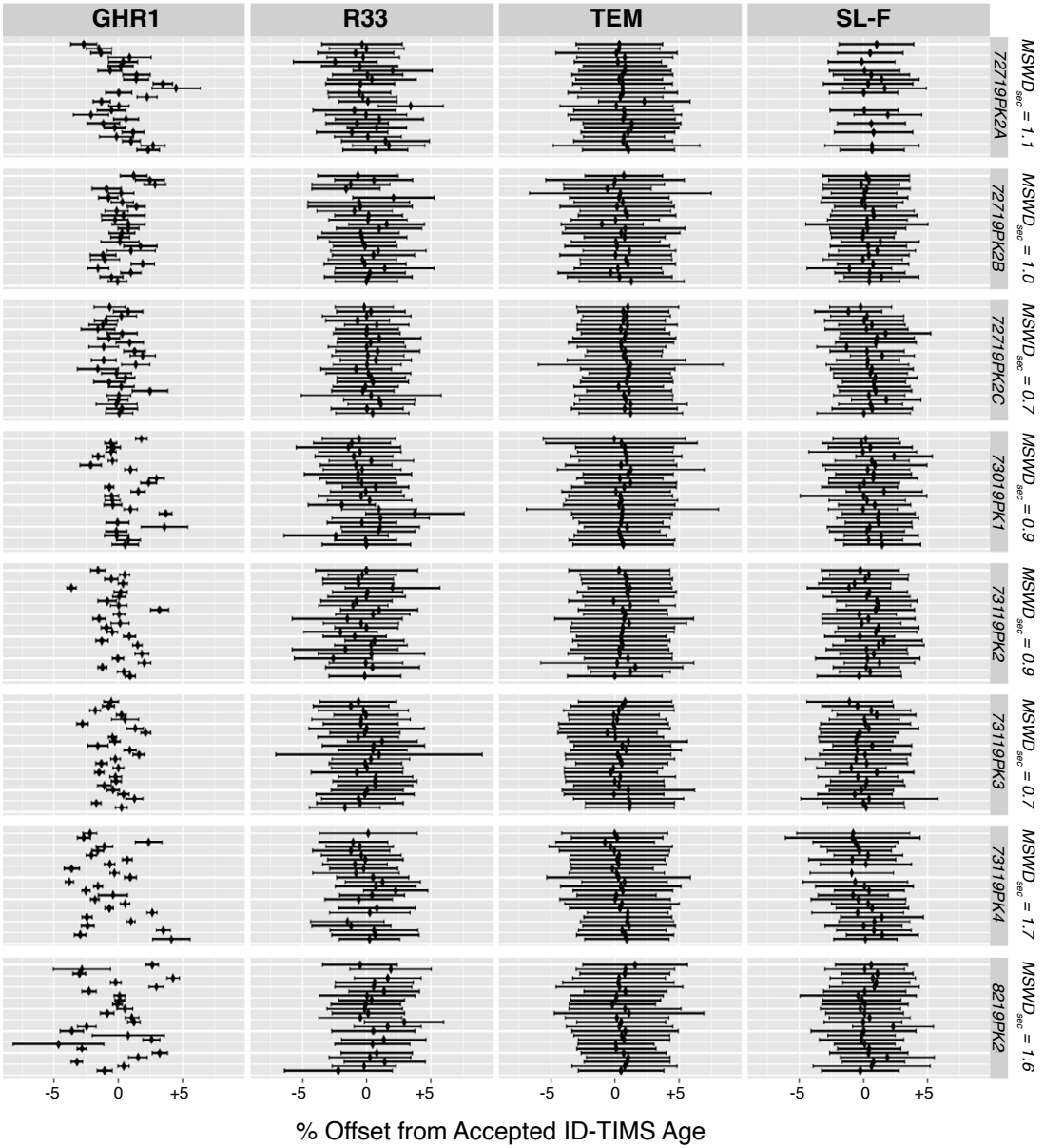

Figure 9. Percent offset from isotope dilution–thermal ionization mass spectrometry (ID-TIMS) ages for secondary reference materials organized vertically by sample run session. Average mean squared weighted deviation (MSWD) of secondary reference materials in each session is listed next to sample name. Note that some reference materials consistently yielded ages slightly older (SL-F, TEM) than the reported ID-TIMS age, but they did not vary systematically together within individual sessions. Mean percent offsets and secondary analyses are reported in Table S3 (see text footnote 1). All uncertainties are reported at 2σ. See secondary reference material descriptions in Zircon Separation, Mount Preparation, and Data Acquisition section in text.

density profiles (PDPs), and zircon age maps overlayed on a CL image base, respectively. We used the PeakFit function of IsoPlotR (Vermeesch, 2018) to deconvolve the youngest distinct but overlapping age populations, while zircon age maps were used to evaluate whether the deconvolution was geologically sound. The deconvolved age populations were texturally distinct in CL images as both rim-core relationships and separate grain populations, so a new weighted mean age was calculated for each population, and the youngest age was deemed to be crystallization age of the rock, while the older (and overlapping) age mode was interpreted to represent inclusion of antecrysts (Miller et al., 2007). This interpretation was supported by both the autocryst and antecryst modes yielding MSWD ~1.

Once a weighted mean age had been assigned, final uncertainties were calculated using the error propagation methods of Horstwood et al. (2016), where uncertainties are divided into (1) internal (or measurement) uncertainties, which indicate the precision of individual measurements, and (2) external (or systematic) uncertainties, which indicate the accuracy of a set of measurements.

For internal uncertainties, we included the uncertainty of the measured $^{206}Pb/^{238}U$ ratio but did not include an overdispersion (excess variance) factor, given that the MSWD value of every set of measurements of primary standards was <1.0. This is documented in Table S2 (see footnote 1) and follows step 5 of Horstwood et al. (2016).

For external uncertainties, we included all the terms in step 8 of Horstwood et al. (2016) as follows:

(1) the ratio uncertainty of the primary RM, which included two components: the uncertainty of the ID-TIMS $^{206}Pb/^{238}U$ ratio of the standard (from published papers), and the uncertainty of the set of measurements used to correct unknowns for fractionation of $^{206}Pb/^{238}U$ (reported in Table S2, see footnote 1), where the latter term is important to the large-*n* approach because it scales inversely with the square root of *n*, with values of 0.3% for a normal-*n* session and values of ~0.05–0.07 for a large-*n* session (2σ);
(2) the long-term variance of validation material, which had a value of 0.20% as determined from analysis of standards during validation experiments conducted between 2019 and 2022 (reported in Table S4);
(3) the decay constant uncertainty (from Jaffey et al., 1971); and
(4) the uncertainty contribution from common Pb correction.

The total systematic uncertainty was calculated from these four terms (five components), added in quadrature because there was little error correlation (see calculation in notes of Table S1, footnote 1).

Increasing the number of unknown analyses from ~25 to ~100 significantly reduced the internal error from ~1% to ~0.3%–0.4% (2σ). Likewise, increasing the number of analyses of the primary RM from ~25 to ~210 also significantly reduced the systematic uncertainty from ~1% to ~0.5%–0.6% (2σ) by minimizing the uncertainty components from the set of measurements used to correct unknowns for fractionation of $^{206}Pb/^{238}U$. The total uncertainty was then calculated as the quadratic sum of the systematic and internal errors, resulting in an average total uncertainty of ~0.5%–0.6% (2σ).

RESULTS

Age results are presented from north to south within the context of crosscutting relationships, as summarized in Table 3. Rim and core relationships are presented based on age determinations and textural zones identified in CL images.

Kitkatla Samples

Foliated Tonalite Host Rock, Sample 72719PK2A

For sample 72719PK2A, 100 analyses on 48 grains yielded a single age mode between 112 and 102 Ma (*n* = 91) from rim analyses, with one older core age of 117 Ma and one mixed rim-core analysis of 223 Ma. We interpret the core material sampled in the mixed analyses to be from a xenocryst, showing the presence of zircon older than 223 Ma in the sample. All grains were euhedral and texturally similar, exhibiting fine oscillatory zoning in

TABLE 3. SAMPLE NAMES, LOCATIONS, DESCRIPTIONS, FABRIC RELATIONS, AGES, AND ANALYTICAL APPROACH

Sample name	Latitude (°N)	Longitude (°W)	Locality	Description	Fabric relations	Age (Ma)	± 2s	*n*	Large-*n*?
72719PK2A	53.767372	130.307814	Kitkatla	Foliated and lineated biotite-hornblende tonalite	Deformed host rock	107	± 0.6	89	Y
72719PK2B	53.767372	130.307814	Kitkatla	Synkinematic biotite-granitoid dike	Crosscuts 72719PK2A	106	± 0.5	92	Y
72719PK2C	53.767372	130.307814	Kitkatla	Fine-grained, weakly foliated, K-feldspar–rich leucocratic dike	Crosscuts 72719PK2A and 72719PK2B	NA	NA	9	Y
73019PK1	53.381204	129.3647	Grenville	Mylonitized garnet-bearing tonalite	Mylonitized host rock	105	± 0.7	18	Y
73119PK1	52.662758	128.53034	Klemtu (Sarah Island)	Undeformed K-feldspar–rich pegmatite dike	Crosscuts 73119PK2	101	± 1	36	N
73119PK2	52.662758	128.53034	Klemtu (Sarah Island)	Mylonitized tonalite with flattened mafic enclaves	Mylonitized host rock	103	± 0.5	92	Y
73119PK3	52.53966	128.494513	Klemtu (Swindle Island)	Mylonitized tonalite with flattened mafic enclaves	Mylonitized host rock	105	± 0.5	83	Y
73119PK4	52.53966	128.494513	Klemtu (Swindle Island)	Weakly deformed biotite-rich granitoid dike	Crosscuts 73119PK3	103	± 0.5	54	Y
8219PK2	52.2643	128.2771	Don Peninsula	Mylonitized coarse-grained biotite-hornblende granitoid sill	Mylonitized host rock	103	± 0.5	90	Y

Note: *n*—number of unknowns analyzed. "Large-*n*?" column signifies whether a sample was analyzed using the large-*n* approach described in the methods. NA—not applicable.

cores truncated by oscillatory zoned rims that were sometimes weakly overprinted by a 25–40-μm-thick homogeneous recrystallization rim. Ages did not correlate with textural domains, and recrystallization rims yielded approximately the same ages as oscillatory zoned rims.

After outlier-rejection, 89 analyses defining the age mode for rims had U concentrations (<800 ppm) and U/Th ratios (generally <6) that did not correlate with age and yielded a weighted mean crystallization age of 106.9 ± 0.6 Ma (2σ, including internal and external uncertainties; MSWD = 0.7; Fig. 10A).

Crosscutting Dike, Sample 72719PK2B

For sample 72719PK2B, 100 analyses on 52 grains yielded an age mode between 112 and 103 Ma (n = 93) from rim analyses and a subordinate age mode between 277 and 256 Ma (n = 3) from core analyses. Major and subordinate ages were measured from different grains. All grains in the younger population exhibited regular oscillatory zoning. Some of these grains also exhibited cores with darker sector zoning and micron-scale bright rims, but these areas were not analyzed. The three grains that yielded the older ages (277–256 Ma) were darker in CL images, exhibited convolute textures, and had micron-scale bright rims.

After outlier-rejection, 92 analyses defining the age mode for rims had U concentrations (generally <600 ppm) and U/Th ratios (generally <10) that did not correlate with age and yielded a weighted mean crystallization age of 106.3 ± 0.5 Ma (MSWD = 1.7; Fig. 10B).

Crosscutting Dike, Sample 72719PK2C

For sample 727219PK2C, 100 analyses on 46 grains yielded three broad age modes. All analyses were conducted on cores because the rims were too small for analysis. We accordingly are not able to report a crystallization age for this sample. Core analyses yielded three groups of ages, 500–480 Ma, 319–274 Ma, and 113–106 Ma. All of these grains are interpreted to be xenocrysts, given that the dike intrudes a rock (sample 72719PK2B) that yielded a zircon U-Pb crystallization age of ca. 106.3 ± 0.5 Ma (sample 72719PK2A).

Grenville Channel Sample

Mylonitized Tonalite, Sample 73019PK1

For sample 73019PK1, 100 analyses on 38 grains yielded a major age mode in rim analyses from 106 to 102 Ma (n = 19) and a large spread of older core ages between 490 and 108 Ma (n = 44). A few grains exhibited homogeneous broad oscillatory zoning and yielded consistent ages from rim to core that represent a subset of the youngest age group (106–104 Ma), but most grains exhibited complex rim-core textures that represent distinct groups of inherited material. Subrounded xenocrystic cores with fine convolute, chaotic, and sector zoning yielded Paleozoic ages significantly older than the youngest rim analyses (mainly mid-Cretaceous, but sometimes late Paleozoic). Larger euhedral cores surrounded by bright 10-μm-scale rims were generally high in U concentration (>1500 ppm), exhibited convolute to chaotic zoning, and yielded consistent ages from 111 to 107 Ma. Irregular domains of low U concentration that cut across concentrically zoned rim-core patterns (localized recrystallization?) yielded the youngest ages between 106 and 104 Ma.

After outlier-rejection, 18 rim analyses defining the youngest age mode had variable U concentrations (135–3400 ppm) and U/Th ratios (generally <8) that did not correlate with age and yielded a weighted mean crystallization age of 104.6 ± 0.7 Ma (MSWD = 0.2; Fig. 10D).

Northern Klemtu Samples

Mylonitic Host, Sample 73119PK2

For sample 73119PK2, 100 analyses on 45 grains yielded a single age mode in rim analyses from 109 to 99 Ma (n = 96) with four older ages of 125–124 Ma from cores. Most grains were euhedral and texturally homogeneous, exhibiting fine oscillatory zoning from rim to core, but a few grains exhibited complex subrounded xenocrystic cores with fine oscillatory zoning that was discordant with the surrounding rim textures. All four of the subordinate ages came from analyses of these cores.

After outlier-rejection, 92 rim analyses had U concentrations (<810 ppm) and U/Th ratios (<4.5) that did not correlate with age and yielded a weighted mean crystallization age of 103.0 ± 0.5 Ma (MSWD = 0.9; Fig. 10E).

Crosscutting Dike, Sample 73119PK1

For sample 73119PK1, 45 analyses on 34 grains yielded a single age mode between 114 and 97 Ma (n = 37) from rims with one older outlier (125 Ma), also from a rim. Zircons were euhedral but texturally complex, exhibiting either broad oscillatory zoning that was very dark in CL images or brighter convolute zones, patchy zones, and irregular zones of recrystallization. Only the darker zones of broad oscillatory zoning yielded calculable ages.

After outlier-rejection, 36 analyses yielded a weighted mean crystallization age of 101.2 ± 1.0 Ma (MSWD = 1.7; Fig. 10F). Uranium concentrations were very high for all analyses (4230–21,370 ppm) and correlated negatively with age, indicating potential Pb-loss (see Supplemental Material, footnote 1). U/Th ratios were low (2–8) and did not correlate with age.

Central Klemtu Samples

Mylonitic Host, Sample 73119PK3

For sample 73119PK3, 100 analyses on 61 grains yielded a single age mode between 113 and 100 Ma (n = 86) from rims, with two older outliers (120 and 125 Ma) from analyses that sampled anomalously dark zones in the rims of crystals with high U concentration (see spot 010 in the Supplemental Material), and three core ages, which were within the age mode of rim analyses (112–104 Ma). Most grains were euhedral and texturally homogeneous,

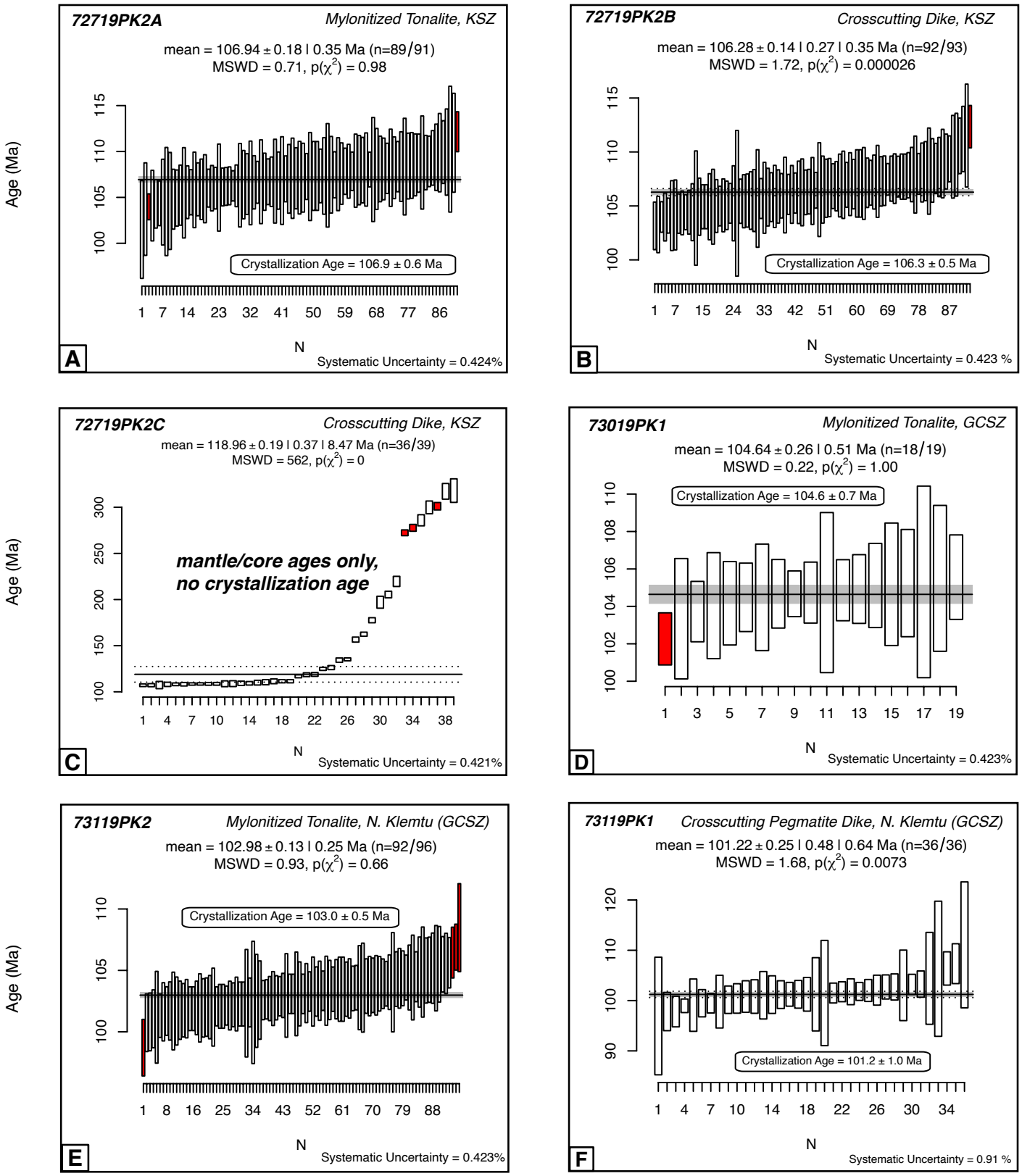

Figure 10. Weighted mean plots organized by shear zone locality from north to south, showing rock type and crosscutting relation, weighted mean age, absolute random uncertainty, percent random uncertainty, mean squared weighted deviation (MSWD), number of analyses included in calculation, percent systematic uncertainty, and final crystallization age after error propagation. White bars are individual analyses ranked by age and presented with 2σ uncertainties. Red bars are individual analyses rejected by IsoplotR (modified Chauvenet's criterion) and not included in the calculation of the weighted mean age due to falling outside of the 2σ confidence interval. All uncertainties are reported at 2σ. KSZ—Kitkatla shear zone; GCSZ—Grenville Channel shear zone.

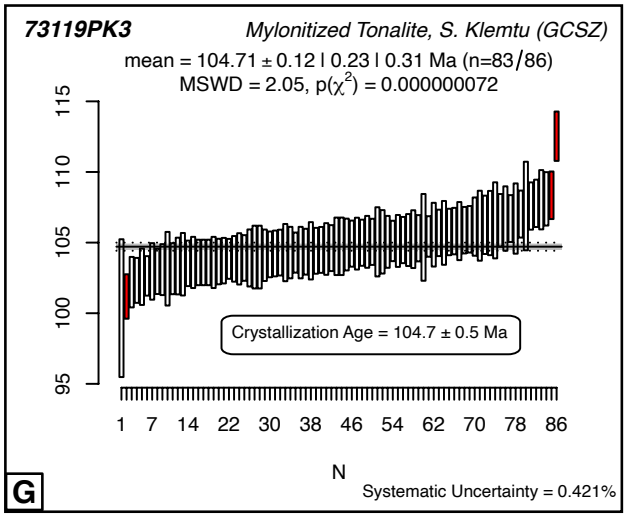

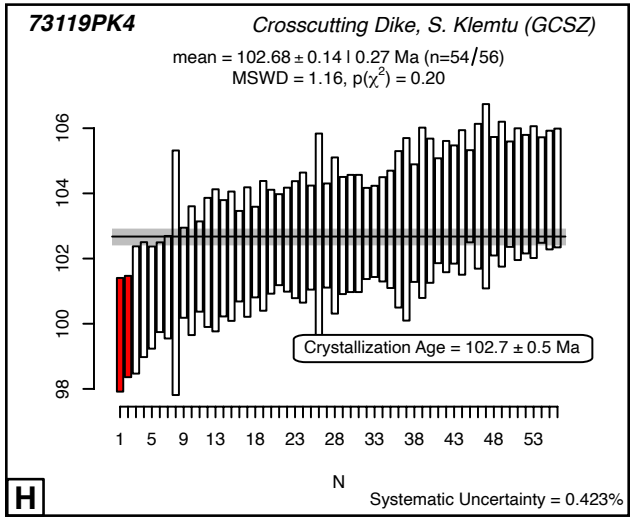

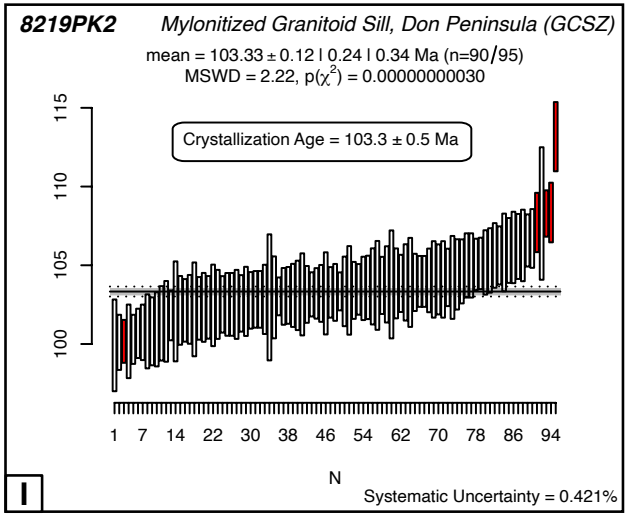

Figure 10 (*continued*).

exhibiting fine oscillatory zoning from rim to core. Some grains contained inclusions and broad dark bands concordant with oscillatory zoning that yielded the oldest ages.

After outlier-rejection, 83 rim analyses yielded a weighted mean crystallization age of 104.7 ± 0.5 Ma (MSWD = 2.1; Fig. 10G). The cause of higher dispersion in the rim analyses is uncertain because there was no correlation between age and Uconc, U/Th, or textural zones in the CL image.

Crosscutting Dike, Sample 73119PK4

For sample 73119PK4, 100 analyses on 49 grains yielded a single age mode between 121 and 100 Ma (n = 99) for rim analyses, with one core age that was within the age mode for rims (117 Ma). Most grains were texturally homogeneous, exhibiting simple oscillatory and sector zoning in CL images, but a few showed evidence of local and late-stage recrystallization (Corfu, 2003). Grains with multiple analyses showed internal variation in age between 1 and 4 m.y. with no clear relationship between age and sampled crystal zone (rim vs. core).

After outlier-rejection, 87 rim analyses yielded a weighted mean age of 103.6 ± 0.3 Ma, and ages were highly dispersed, with an MSWD of 4.4. U concentrations of individual analyses spanned a wide range (109–1612 ppm) but did not vary systematically with age, so Pb loss is an unlikely source for the overdispersion. The incorporation of xenocrysts can also be ruled out based on the overall textural homogeneity between rims and cores of grains in this group. This leaves recycling of antecrysts as a likely explanation, which is supported by textural evidence of recrystallization as well as two overlapping but distinct age populations defined by analyses with ages between 108 and 100 Ma (as shown in the probability density plot of rim ages; see Supplemental Material, footnote 1). Deconvolving the 108–100 Ma rim analyses using the PeakFit function of IsoplotR (Galbraith and Laslett, 1993; Vermeesch, 2018) yielded a final crystallization age of 102.7 ± 0.5 Ma (MSWD = 1.2, n = 54; Fig. 10H) and an older antecryst mode that yielded a weighted mean age of 105.9 ± 0.6 Ma (MSWD = 1.6, n = 31).

Southern Klemtu Samples (Don Peninsula)

Coarse-Grained Mylonitic Sill, Sample 8219PK2

For sample 8219PK2, 100 analyses on 49 grains yielded a single age mode between 113 and 100 Ma (n = 95) from rim analyses. Most grains were texturally simple and exhibited homogeneous oscillatory zoning from rim to core. A few grains exhibited recrystallization textures, truncated internal zoning, unzoned cores, or internal convolute textures, but none of these features correlated systematically with age.

After outlier-rejection, 90 rim analyses had low U concentrations (generally <1000 ppm) and U/Th ratios (2–6) that did not correlate with age and yielded a crystallization age of 103.3 ± 0.5 Ma (MSWD = 2.2; Fig. 10I) for the mylonitic sill. Although the MSWD is >1, deconvolving the data set did not produce distinct age populations with any geologic basis in CL images.

DISCUSSION

Higher-precision zircon U-Pb ages for pre-, syn-, and postkinematic intrusions in the interlinked Kitkatla and Grenville Channel shear zones provide new insights into the timing of sinistral strike-slip tectonics in the Canadian Cordillera and indicate how strike-slip deformation was partitioned in a growing magmatic arc during oblique convergence. We discuss implications for large-scale intraterrane displacement based on previously hypothesized piercing points but recognize the limitations in our data set that preclude resolution of these issues completely.

Timing of Sinistral Shear Zone Deformation

Kitkatla Shear Zone

Samples of syn- to late-kinematic intrusions from a single locality within the Kitkatla shear zone show that local deformation was linked to magma emplacement over a short duration, with a 106.9 ± 0.6 Ma mylonitized tonalite (72719PK2A) cut by a weakly deformed 106.3 ± 0.5 Ma late-kinematic dike (72719PK2B; Fig. 5A). Previously published data indicate that shear zone deformation was active in other parts of the Kitkatla shear zone prior to 107 Ma. Butler et al. (2006) reported crystallization ages of 113 Ma for a synkinematic intrusion in the western portion of the shear zone and an age of 107.5 ± 1.5 Ma for a posttectonic dike crosscutting the shear zone fabric near our sampling area. Tochilin et al. (2014) reported a maximum depositional age of 119 Ma for conglomerates that may have formed in a pull-apart basin related to deformation along the Kitkatla shear zone. Collectively, available data bracket the age of deformation within the Kitkatla shear zone to between 119 and 106.2 ± 0.5 Ma (Fig. 11). The initiation age of shear zone deformation remains to be constrained.

Grenville Channel Shear Zone

Four new ages from within the Grenville Channel shear zone indicate that deformation occurred between 105 and 101 Ma during intrusion of local granitoids and tonalites. At the northernmost locality from the southwest shore of Grenville Channel, a mylonitized granitoid intrusion with sinistral strike-slip S-C fabrics yielded a crystallization age of 104.6 ± 0.7 Ma (73019PK1). This age is consistent with Lu-Hf ages of 108–102 Ma reported by Wolf et al. (2010) for synkinematic garnet growth in the region. On Sarah Island, a few kilometers north of Klemtu, a 103.0 ± 0.5 Ma mylonitized tonalite (73119PK2) is cut by a weakly deformed 101.2 ± 1.0 Ma late-kinematic dike (73119PK1; Figs. 4 and 5B), and on Swindle Island, 15 km to the south, a 104.7 ± 0.5 Ma mylonitized tonalite (73119PK3) is cut by an undeformed 102.7 ± 0.5 Ma pegmatite dike (73119PK4; Figs. 4 and 5C). At the southernmost locality, a mylonitic sill on Don Peninsula yielded a crystallization age of 103.3 ± 0.3 Ma (8219PK1); this sill displayed magmatic-state subhorizontal mineral lineations overprinted by solid-state brittle-ductile sinistral S-C fabrics (Figs. 4 and 7B). These relations show that Grenville Channel shear zone deformation was active at 108 Ma and terminated by 101 Ma (Fig. 11). The

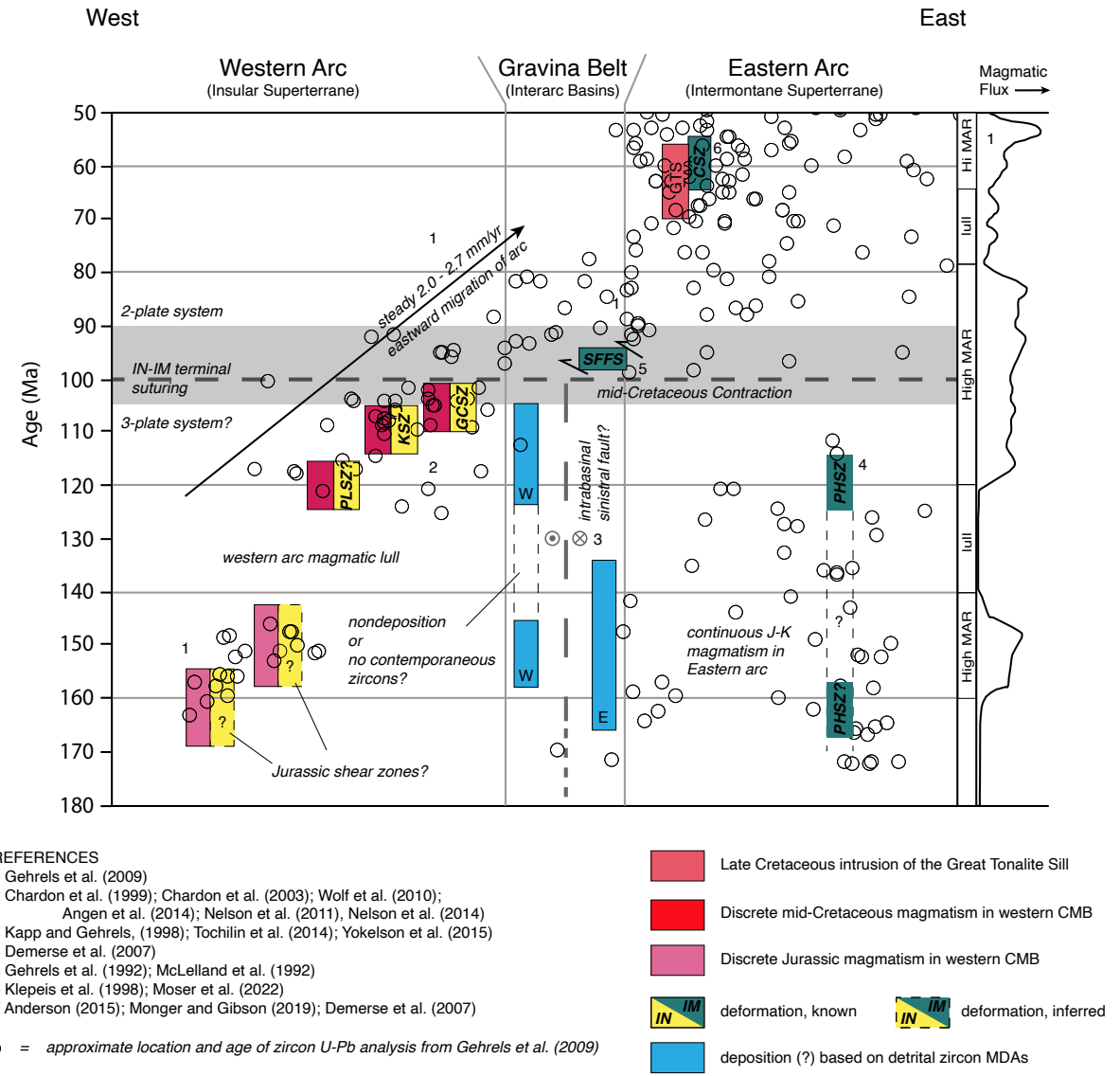

REFERENCES
1 Gehrels et al. (2009)
2 Chardon et al. (1999); Chardon et al. (2003); Wolf et al. (2010); Angen et al. (2014); Nelson et al. (2011), Nelson et al. (2014)
3 Kapp and Gehrels, (1998); Tochilin et al. (2014); Yokelson et al. (2015)
4 Demerse et al. (2007)
5 Gehrels et al. (1992); McLelland et al. (1992)
6 Klepeis et al. (1998); Moser et al. (2022)
7 Anderson (2015); Monger and Gibson (2019); Demerse et al. (2007)

○ = *approximate location and age of zircon U-Pb analysis from Gehrels et al. (2009)*

Late Cretaceous intrusion of the Great Tonalite Sill
Discrete mid-Cretaceous magmatism in western CMB
Discrete Jurassic magmatism in western CMB
IN IM deformation, known
IN IM deformation, inferred
deposition (?) based on detrital zircon MDAs

Figure 11. Space-time-geology diagram highlighting interplay between deformation and magmatism in the midcoast region. Abbreviations: CMB—Coast Mountains Batholith; IN—Insular superterrane; IM—Intermontane superterrane; SFFS—Sumdum-Fanshaw fault system; PLSZ—Principe-Laredo shear zone; KSZ—Kitkatla shear zone; GCSZ—Grenville Channel shear zone; PHSZ—Pootlass high-strain zone; GTS—Great Tonalite Sill; CSZ—Coast shear zone; W—western Gravina; E—eastern Gravina; J-K—Jurassic–Cretaceous; MAR—magmatic addition rates. Yellow boxes—shear zones rooted in the Insular superterrane; green boxes—shear zones rooted in the Intermontane superterrane; red boxes—discrete episodes of magmatism; blue boxes—age range of deposition in the Gravina basin inferred from detrital zircon MDAs. MDA—maximum depositional age. Numbers correspond to groups of references in the figure key.

presence of younger deformed dikes with orientations and strain markers indicative of sinistral shear at the northern end of Grenville Channel (Fig. 4) may indicate that regional sinistral shear zone deformation continued as late as 97 Ma (Angen et al., 2014), but it could also reflect a more local event related to intrusion of the adjacent Ecstall pluton (Chardon, 2003; Wolf et al., 2010). The age of initiation of activity on the Grenville Channel shear zone is unknown but may have occurred by 123 Ma, based on a zircon U-Pb age for a synkinematic(?) intrusion ~15 km ESE of Klemtu (Nelson et al., 2011).

Magma-Enhanced Deformation

Crosscutting relations at three localities (Fig. 5) between Kitkatla and Klemtu show that sinistral deformation in the western Coast Mountains Batholith was spatially and temporally linked to a major phase of intrusive arc magmatism from ca. 107 to 101 Ma. At any given locality, crystallization ages of deformed granitoids and crosscutting dikes are within ~0.7–2 m.y. of one another, suggesting that deformation was synmagmatic and ended within 0.7–2 m.y. of comagmatic intrusion crystallization. Subvertical intra-arc shear zones facilitate and are enhanced by magma emplacement (e.g., de Saint Blanquat and Tikoff, 1997; Hutton, 1997), and these closely overlapping crosscutting relations may well reflect "magma-facilitated strike-slip partitioning" (de Saint Blanquat et al., 1998), where deformation was spatially and temporally linked to sites of active intrusion and vice versa. The preservation of magmatic-state subhorizontal mineral lineations weakly overprinted by protomylonitic sinistral S-C fabrics within a 104 Ma shear zone intrusion (8219PK2; see aligned albite twins in Fig. 7B) at the southern end of the Grenville Channel shear zone (Don Peninsula) further illustrates this point.

The timing of shear zone deformation appears to decrease in age from west to east, following the regional trend of eastward-younging magmatism in the Cretaceous western arc (magma-enhanced deformation at ca. 113–106 Ma in the Kitkatla shear zone terminated at 106.2 ± 0.5 Ma compared to termination ca. 105–103.3 ± 0.5 Ma in the Grenville Channel shear zone; Fig. 11). Thus, the lateral migration of strike-slip deformation and arc magmatism were also linked.

We attribute the midcoast shear zones to strike-slip partitioning in the upper plate of an obliquely convergent subduction margin, where strike-parallel motion was partitioned into the thermally weak arc (e.g., de Saint Blanquat et al., 1998). The structural and geochronologic links between intrusion and major transcurrent shear zone deformation suggest that plate convergence was oblique between at least 113 and 101 Ma, similar to the modern Sumatran ocean-continent convergent margin, where the Great Sumatran intra-arc dextral strike-slip fault accommodates approximately one third of the tangential component of plate motion (Tikoff and Teyssier, 1994; de Saint Blanquat et al., 1998).

Regional Significance of Shear Zone Timing

Crystallization ages of 107–103 Ma for pre-(?) to synkinematic intrusions and 106–101 Ma for comagmatic crosscutting dikes from five localities along the ~250-km-long along-strike shear zone transect of this study indicate that sinistral deformation in the western Coast Mountains Batholith was active during and ended with the last major intrusive phase from 107 to 101 Ma. Recent plate motion reconstructions by Müller et al. (2016) and Merdith et al. (2020) show that the western margin of North America was migrating west without much latitudinal variation between ca. 110 and 100 Ma, suggesting that trench-parallel motion of the outboard oceanic plate (Farallon/Kula?) was the main driver of sinistral strike-slip partitioning within the arc, due to a NW-SE–oriented plate margin and/or SE-directed oblique subduction of the ancient oceanic plate. Future plate motion reconstructions for the Canadian Cordillera should include mid-Cretaceous sinistral motion from at least 107 to 101 Ma, and possibly earlier.

This sinistral deformation preceded a major phase of mid- to Late Cretaceous shortening recorded throughout the Coast Mountains (Journeay and Friedman, 1993; Rusmore and Woodsworth, 1994; Schiarizza et al., 1997) and an eastward migration in more voluminous magmatism (Gehrels et al., 2009; Cecil et al., 2018), marking a change from sinistral-oblique to orthogonal plate convergence starting at ca. 100 Ma (Fig. 11). This timing also aligns with the collapse of the Gravina belt, the southernmost known extent of which, southwest of Bella Coola, lies <20 km inboard of the Grenville Channel shear zone (Fig. 4).

The Gravina belt is interpreted to be a collapsed backarc basin to the western Coast Mountains Batholith because of its position relative to the arc and a strong correlation between age modes in the detrital zircon record and the igneous crystallization history of the western Coast Mountains Batholith (Yokelson et al., 2015). Gravina belt deposition ended between 112 and 105 Ma, after which the basin was structurally inverted between 105 and 90 Ma (McClelland et al., 1992; Kapp and Gehrels, 1998; Yokelson et al., 2015). Basin strata are variably metamorphosed and structurally disrupted between the western and eastern arcs, as documented by Gehrels et al. (2009), where they are involved in a west-vergent thrust belt of mid-Cretaceous age that structurally juxtaposes them below plutonic and metasedimentary rocks of the Taku, Yukon-Tanana, and Stikine (Intermontane) terranes (the Sumdum-Fanshaw fault system of Figs. 4 and 11). Thus, the contemporaneous cessation of sinistral shear zones in the western Coast Mountains Batholith, onset of structural inversion of the Gravina basin, and inboard jump in magmatism may represent the terminal suturing between the Insular and Intermontane superterranes at ca. 100 Ma (McGroder, 1991; Journeay and Friedman, 1993; Rusmore and Woodsworth, 1994; Gehrels et al., 2009). Mid- to lower-crustal deformation also migrated to the east with magmatism, localizing most strongly in the subvertical Coast shear zone/Great Tonalite Sill between ca. 80 and 55 Ma (Ingram and Hutton, 1994; Klepeis et al., 1998; Rusmore et al., 2001).

Implications for Models of Large-Scale Intraterrane Transport

Our data agree with existing plate motion models (Monger and Gibson, 2019) for the Canadian

Cordillera that show significant sinistral-oblique convergence in Early Cretaceous time, but our results extend the timing until ca. 101 Ma (Figs. 2 and 11). Tectonic models and hypotheses for sinistral offsets in the Canadian Cordillera predict total displacements ranging from 600 to 1000 km anytime between Middle Jurassic and Late Cretaceous time (Plafker et al., 1989; Monger et al., 1994; Plafker and Berg, 1994; Umhoefer et al., 2002; Umhoefer, 2003; Gehrels et al., 2009; Tochilin et al., 2014; Anderson, 2015). The shear zones of this study are of the appropriate age and position to have accommodated some of this motion, but probably not all of it. Using the earliest reported age of initiation for sinistral shear zones in the region, ca. 123 Ma (Nelson et al., 2011), and a termination age of ca. 101 Ma (this study), calculations require sinistral displacements rates of ~36 mm/yr to accommodate 800 km of motion. Even the modern Andaman Sea accommodates only 40 mm/yr of strike-slip motion at most, and the convergence angle is so low that little to no surface magmatism occurs (Curray et al., 1979; de Saint Blanquat et al., 1998). The shear zones of this study are intraplate shear zones that occurred in association with an arc and most likely accommodated only a fraction of the plate-tangential motion during oblique convergence (Tikoff and Teyssier, 1994). For comparison, the Great Sumatran fault (a modern intra-arc fault) accommodates ~10–15 mm/yr of plate-tangential motion. If the shear zones of this study are comparable, ~80–53 m.y. of continuous deformation would be required to achieve 800 km of coastwise translation within the arc alone. If paleomagnetic and paleobiogeographic displacement estimates are correct, and the sinistral motion occurred mainly in the mid-Cretaceous, contemporaneous sinistral faults in the forearc and backarc regions (that were subsequently consumed by subduction erosion, were overprinted by later magmatism, or are as-yet unidentified) would have been needed to accommodate the full amount of motion.

It is also possible that an earlier phase (or initiation) of sinistral shear zones in Middle to Late (?) Jurassic time accommodated some of the total post-Triassic displacements (Anderson, 2015; Monger and Gibson, 2019). Continuous sinistral-oblique convergence initiating at ca. 160 Ma and ending at ca. 101 Ma is permissible with the available evidence and allows reasonable intraplate deformation rates to have accommodated 800 km of southward coastwise displacement. It is difficult to confirm whether such a prolonged period of sinistral-oblique convergence occurred because there is no magmatic record between 142 and 118 Ma (the Early Cretaceous magmatic lull of the western Coast Mountains Batholith), and thus there is no intra-arc record of plate-motion obliquity (Fig. 11). The Early Cretaceous magmatic lull may also be interpreted as the product of extremely low convergence angles, where sinistral strike-slip motion was the dominant kinematic regime (Gehrels et al., 2009), similar to the modern Andaman Sea region of the Sumatran subduction zone.

The shear zones of this study are rooted within rocks of the Insular superterrane, so their motion has no bearing on the >800 km of left-lateral interterrane displacement proposed by Monger et al. (1994) and Umhoefer et al. (2002) to explain juxtaposition of forearc and backarc basin assemblages in the southern Coast Mountains. The timing does, however, align well with other mid-Cretaceous sinistral-oblique structures in the Intermontane terrane (Hurlow, 1993; Schiarizza et al., 1997; Evenchick, 2001; Israel et al., 2006; Demerse et al., 2007), suggesting that the Insular and Intermontane terranes may have been kinematically linked prior to their terminal collision at 100 Ma. The Pasayten magma-enhanced sinistral shear zone (Fig. 3) was active between 109 and 95 Ma within the Okanagan Range batholith (Greig, 1992; Hurlow, 1993; Hurlow and Nelson, 1993), a composite Jurassic–Cretaceous sheeted intrusive suite that was emplaced into Intermontane basement (Stikine and Quesnel). The Pootlass high-strain zone near Bella Coola (Figs. 3 and 11) includes mylonitized Jurassic tonalites with sinistral S-C fabrics that intrude metasedimentary rocks of the Stikine terrane and are crosscut by ca. 114 Ma postkinematic felsic dikes (Demerse et al., 2007). The presence of these intra-arc shear zone systems in both outboard and inboard terranes suggests that sinistral transpression was the dominant kinematic regime during the Early Cretaceous (and Middle to Late Jurassic?) Coast-Cascade orogeny, and it involved multiple subparallel subduction zone–arc systems that underwent similar strain. It is also possible that the shear zones of this study and the Pasayten shear zone were once continuously linked in the same magmatic arc, requiring significant post–100 Ma sinistral offset in the southern Coast Mountains, for which there is some geologic evidence (Monger et al., 1994; Israel et al., 2006, 2013; Israel, 2008).

CONCLUSIONS

Large intra-arc shear zones localized in the western Coast Mountains Batholith record sinistral-oblique convergence in the Canadian Cordillera that lasted from at least 114 to 101 Ma, but which may have begun much earlier (during Late Jurassic time?). Shear zone deformation was temporally and spatially linked to arc magmatism, which is illustrated by (1) petrographic observations of magmatic-state (i.e., hypersolidus/pre–full crystallization) fabrics, (2) the overlap in crosscutting ages of syn- and postkinematic intrusions, and (3) the apparent linked migration of shear zone deformation and magmatism to the east. Employment of a new large-*n* igneous zircon U-Pb strategy more than doubled the precision of measurements obtained by LA-ICP-MS and allowed us to demonstrate the close relation between magmatism and deformation by dating comagmatic crosscutting phases. Findings of regional ≥114 Ma to ca. 101 Ma sinistral shear zones in the Insular terrane of midcoast British Columbia support paleogeographic models invoking major sinistral-oblique convergence in the Canadian Cordillera prior to east-west shortening and orogenic development beginning at ca. 100 Ma. These timing constraints also align with other sinistral shear zones rooted in the eastern Coast Mountains, suggesting that the Insular and Intermontane superterranes may have been kinematically linked as early as 114 Ma. Further work is still needed to constrain the regional extent, total displacement magnitude, and initiation age(s) of sinistral shear zones in the Coast Mountains Batholith.

DATA AVAILABILITY

Zircon U-Pb data and corresponding cathodoluminescence images presented in this paper are available in the Supplemental Material (see footnote 1). All structural measurements, field photographs, and microstructural information are available through StraboSpot (https://www.strabospot.org/search/).

ACKNOWLEDGMENTS

This research was funded by National Science Foundation (NSF) grant EAR- 818509 and was partially supported by NSF/Geological Society of America Graduate Student Geoscience grant 12951–20, which is funded by NSF Award 1949901. Laboratory funding to the Arizona LaserChron Center was provided by NSF grant EAR-1649254. We thank M. Pecha, N. Geissler, and the University of Arizona LaserChron Center for laboratory assistance. We also thank Andrew Kylander-Clark, Nancy Riggs, and an anonymous reviewer for insightful and constructive reviews.

REFERENCES CITED

Anderson, T.H., 2015, Jurassic (170–150 Ma) basins: The tracks of a continental-scale fault, the Mexico-Alaska megashear, from the Gulf of Mexico to Alaska, *in* Anderson, T.H., Didenko, A., Johnson, C., Khanchuk, A., and MacDonald, J., eds., Late Jurassic Margin of Laurasia—A Record of Faulting Accommodating Plate Rotation: Geological Society of America Special Paper 513, p. 107–188, https://doi.org/10.1130/2015.2513(03).

Angen, J.J., Van Staal, C.R., Lin, S., Nelson, J.L., Mahoney, J.B., Davis, D.W., and McClelland, W.C., 2014, Kinematics and timing of shear zone deformation in the western Coast belt: Evidence for mid-Cretaceous orogen-parallel extension: Journal of Structural Geology, v. 68, p. 273–299, https://doi.org/10.1016/j.jsg.2014.05.026.

Beck, M.E., Jr., 1991, Case for northward transport of Baja and coastal southern California: Paleomagnetic data, analysis, and alternatives: Geology, v. 19, no. 5, p. 506–509, https://doi.org/10.1130/0091-7613(1991)019<0506:CFNTOB>2.3.CO;2.

Berg, H.C., Jones, D.L., and Richter, D.H., 1972, Gravina-Nutzotin belt—Tectonic significance of an Upper Mesozoic sedimentary and volcanic sequence in southern and southeastern Alaska: U.S. Geological Survey Research 1972, Chapter D: U.S. Geological Survey Professional Paper 800-D, p. D1–D24, https://doi.org/10.3133/pp800D.

Black, L.P., Kamo, S.L., Allen, C.M., Davis, D.W., Aleinikoff, J.N., Valley, J.W., Mundil, R., Campbell, I.H., Korsch, R.J., and Williams, I.S., 2004, Improved $^{206}Pb/^{238}U$ microprobe geochronology by the monitoring of a trace-element–related matrix effect; SHRIMP, ID-TIMS, ELA-ICP-MS and oxygen isotope documentation for a series of zircon standards: Chemical Geology, v. 205, no. 1–2, p. 115–140, https://doi.org/10.1016/j.chemgeo.2004.01.003.

Butler, R., Gehrels, G., Hart, W., Davidson, C., Crawford, M., Haggart, J., Enkin, R., and Monger, J., 2006, Paleomagnetism of Late Jurassic to mid-Cretaceous plutons near Prince Rupert, British Columbia, *in* Haggart, J.W., Enkin, R.J., and Monger, J.W.H., eds., Paleogeography of the North American Cordillera: Evidence For and Against Large-Scale Displacements: Geological Association of Canada Special Paper 46, p. 171–200.

Carter, E.S., and Haggart, J.W., 2006, Radiolarian biogeography of the Pacific region indicates a mid- to high-latitude (>30°) position for the Insular superterrane since the late Early Jurassic, *in* Haggart, J.W., Enkin, R.J., and Monger, J.W.H., eds., Paleogeography of the North American Cordillera: Evidence For and Against Large-Scale Displacements: Geological Association of Canada Special Paper 46, p. 109–132.

Cecil, M., Rusmore, M., Gehrels, G.E., Woodsworth, G., Stowell, H., Yokelson, I., Chisom, C., Trautman, M., and Homan, E., 2018, Along-strike variation in the magmatic tempo of the Coast Mountains batholith, British Columbia, and implications for processes controlling episodicity in arcs: Geochemistry, Geophysics, Geosystems, v. 19, no. 11, p. 4274–4289, https://doi.org/10.1029/2018GC007874.

Chardon, D., 2003, Strain partitioning and batholith emplacement at the root of a transpressive magmatic arc: Journal of Structural Geology, v. 25, no. 1, p. 91–107, https://doi.org/10.1016/S0191-8141(02)00015-9.

Chardon, D., Andronicos, C.L., and Hollister, L.S., 1999, Large-scale transpressive shear zone patterns and displacements within magmatic arcs: The Coast plutonic complex, British Columbia: Tectonics, v. 18, no. 2, p. 278–292, https://doi.org/10.1029/1998TC900035.

Clennett, E.J., Sigloch, K., Mihalynuk, M.G., Seton, M., Henderson, M.A., Hosseini, K., Mohammadzaheri, A., Johnston, S.T., and Müller, R.D., 2020, A quantitative tomotectonic plate reconstruction of western North America and the eastern Pacific basin: Geochemistry, Geophysics, Geosystems, v. 21, https://doi.org/10.1029/2020GC009117.

Corfu, F., 2003, Atlas of zircon textures: Reviews in Mineralogy and Geochemistry, v. 53, no. 1, p. 469–500, https://doi.org/10.2113/0530469.

Cowan, D.S., Brandon, M.T., and Garver, J.I., 1997, Geologic tests of hypotheses for large coastwise displacements—A critique illustrated by the Baja British Columbia controversy: American Journal of Science, v. 297, no. 2, p. 117–173, https://doi.org/10.2475/ajs.297.2.117.

Cui, Y., Miller, D., Schiarizza, P., and Diakow, L.J., 2017, British Columbia digital geology: British Columbia Ministry of Energy, Mines and Petroleum Resources, British Columbia Geological Survey Open File 2017-8.

Curray, J., Moore, D., Lawver, L., Emmel, F., Raitt, R., Henry, M., and Kieckhefer, R., 1979, Tectonics of the Andaman Sea and Burma: Convergent margins, *in* Watkins, J.S., Montadert, L., and Dickerson, P.W., eds., Geological and Geophysical Investigations of Continental Margins: American Association of Petroleum Geologists Memoir 29, p. 189–198, https://doi.org/10.1306/M29405C12.

Dafov, M.N., Carrera, A., Gehrels, G.E., Alberts, D., Pereira, M., Cecil, M.R., Rusmore, M.E., Stowell, H.H., and Woodsworth, G.J., 2020, U-Th-Pb geochronology and Lu-Hf isotope geochemistry of detrital zircons in metasedimentary rocks of the Southern Coast Mountains Batholith: Lithosphere, v. 2020, no. 1, https://doi.org/10.2113/2020/8854686.

Demerse, D., Kennedy, L., Ullrich, T., and Mortensen, J., 2007, The Pootlass high strain zone, Bella Coola BC: Timing, kinematics and significance: San Francisco, California, American Geophysical Union, Fall Meeting supplement, abstract T11B–0575.

de Saint Blanquat, M., and Tikoff, B., 1997, Development of magmatic to solid-state fabrics during syntectonic emplacement of the Mono Creek Granite, Sierra Nevada Batholith, *in* Bouchez, J.L., Hutton, D.H.W., and Stephens, W.E., eds., Granite: From Segregation of Melt to Emplacement Fabrics: Dordrecht, Netherlands, Springer, p. 231–252, https://doi.org/10.1007/978-94-017-1717-5_15.

de Saint Blanquat, M., Tikoff, B., Teyssier, C., and Vigneresse, J.L., 1998, Transpressional kinematics and magmatic arcs, *in* Holdsworth, R.E., Strachan, R.A., and Dewey, J.F., eds., Continental Transpressional and Transtensional Tectonics: Geological Society, London, Special Publication 135, p. 327–340, https://doi.org/10.1144/GSL.SP.1998.135.01.21.

D'Iemos, R., Brown, M., and Strachan, R., 1992, Granite magma generation, ascent and emplacement within a transpressional orogen: Journal of the Geological Society, v. 149, no. 4, p. 487–490, https://doi.org/10.1144/gsjgs.149.4.0487.

Eddy, M.P., Ibañez-Mejia, M., Burgess, S.D., Coble, M.A., Cordani, U.G., DesOrmeau, J., Gehrels, G.E., Li, X., MacLennan, S., and Pecha, M., 2019, GHR 1 zircon—A new Eocene natural reference material for microbeam U-Pb geochronology and Hf isotopic analysis of zircon: Geostandards and Geoanalytical Research, v. 43, no. 1, p. 113–132, https://doi.org/10.1111/ggr.12246.

Enkin, R., 2006, Paleomagnetism and the case for Baja British Columbia, *in* Haggart, J.W., Enkin, R.J., and Monger, J.W.H., eds., Paleogeography of the North American Cordillera: Evidence For and Against Large-Scale Displacements: Geological Association of Canada Special Paper 46, p. 233–253.

Evenchick, C.A., 2001, Northeast-trending folds in the western Skeena fold belt, northern Canadian Cordillera: A record of Early Cretaceous sinistral plate convergence: Journal of Structural Geology, v. 23, no. 6–7, p. 1123–1140, https://doi.org/10.1016/S0191-8141(00)00178-4.

Galbraith, R.F., and Laslett, G.M., 1993, Statistical models for mixed fission track ages: Nuclear Tracks and Radiation Measurements, v. 21, no. 4, p. 459–470, https://doi.org/10.1016/1359-0189(93)90185-C.

Garver, J.I., and Davidson, C.M., 2015, Southwestern Laurentian zircons in upper Cretaceous flysch of the Chugach-Prince William terrane in Alaska: American Journal of Science, v. 315, no. 6, p. 537–556, https://doi.org/10.2475/06.2015.02.

Gehrels, G., and Pecha, M., 2014, Detrital zircon U-Pb geochronology and Hf isotope geochemistry of Paleozoic and Triassic passive margin strata of western North America: Geosphere, v. 10, no. 1, p. 49–65, https://doi.org/10.1130/GES00889.1.

Gehrels, G.E., McClelland, W.C., Samson, S.D., Patchett, P.J., and Orchard, M.J., 1992, Geology of the western flank of the Coast Mountains between Cape Fanshaw and Taku Inlet, southeastern Alaska: Tectonics, v. 11, no. 3, p. 567–585, https://doi.org/10.1029/92TC00482.

Gehrels, G., Rusmore, M., Woodsworth, G., Crawford, M., Andronicos, C., Hollister, L., Patchett, J., Ducea, M., Butler, R., and Klepeis, K., 2009, U-Th-Pb geochronology of the Coast Mountains batholith in north-coastal British Columbia: Constraints on age and tectonic evolution: Geological Society of America Bulletin, v. 121, no. 9–10, p. 1341–1361, https://doi.org/10.1130/B26404.1.

Gehrels, G.E., 2001, Geology of the Chatham Sound region, southeast Alaska and coastal British Columbia: Canadian Journal of Earth Sciences, v. 38, no. 11, p. 1579–1599, https://doi.org/10.1139/e01-040.

Gehrels, G.E., and Boghossian, N.D., 2000, Reconnaissance geology and U-Pb geochronology of the west flank of the Coast Mountains between Bella Coola and Prince Rupert, coastal British Columbia, *in* Stowell, H.H., and McClelland, W.C., eds., Tectonics of the Coast Mountains, Southeastern Alaska and British Columbia: Geological Society of America Special Paper 343, p. 61–75, https://doi.org/10.1130/0-8137-2343-4.61.

Gehrels, G.E., Valencia, V.A., and Ruiz, J., 2008, Enhanced precision, accuracy, efficiency, and spatial resolution of U-Pb ages by laser ablation–multicollector–inductively coupled plasma–mass spectrometry: Geochemistry, Geophysics, Geosystems, v. 9, no. 3, https://doi.org/10.1029/2007GC001805.

Greig, C.J., 1992, Jurassic and Cretaceous plutonic and structural styles of the Eagle plutonic complex, southwestern British Columbia, and their regional significance: Canadian Journal of Earth Sciences, v. 29, no. 4, p. 793–811, https://doi.org/10.1139/e92-067.

Horstwood, M.S., Košler, J., Gehrels, G., Jackson, S.E., McLean, N.M., Paton, C., Pearson, N.J., Sircombe, K., Sylvester, P., and Vermeesch, P., 2016, Community-derived standards for LA-ICP-MS U-(Th-) Pb geochronology—Uncertainty propagation, age interpretation and data reporting: Geostandards and Geoanalytical Research, v. 40, no. 3, p. 311–332, https://doi.org/10.1111/j.1751-908X.2016.00379.x.

Hurlow, H.A., 1993, Mid-Cretaceous strike-slip and contractional fault zones in the western Intermontane terrane, Washington, and their relation to the North Cascades–Southeastern Coast belt orogen: Tectonics, v. 12, no. 5, p. 1240–1257, https://doi.org/10.1029/93TC01061.

Hurlow, H.A., and Nelson, B.K., 1993, U-Pb zircon and monazite ages for the Okanogan Range batholith, Washington: Implications for the magmatic and tectonic evolution of the southern Canadian and northern United States Cordillera: Geological Society of America Bulletin, v. 105, no. 2, p. 231–240, https://doi.org/10.1130/0016-7606(1993)105<0231:UPZAMA>2.3.CO;2.

Hutton, D.H.W., 1988, Granite emplacement mechanisms and tectonic controls: Inferences from deformation studies: Earth and Environmental Science Transactions of the Royal Society of Edinburgh, v. 79, no. 2–3, p. 245–255, https://doi.org/10.1017/S0263593300014255.

Hutton, D.H.W., 1997, Syntectonic granites and the principle of effective stress: A general solution to the space problem?, *in* Bouchez, J.L., Hutton, D.H.W., and Stephens, W.E., eds., Granite: From Segregation of Melt to Emplacement Fabrics: Dordrecht, Netherlands, Springer, p. 189–197, https://doi.org/10.1007/978-94-017-1717-5_12.

Hutton, D.H.W., and Reavy, R.J., 1992, Strike-slip tectonics and granite petrogenesis: Tectonics, v. 11, no. 5, p. 960–967, https://doi.org/10.1029/92TC00336.

Ingram, G.M., and Hutton, D.H., 1994, The Great Tonalite Sill: Emplacement into a contractional shear zone and implications for Late Cretaceous to early Eocene tectonics in southeastern Alaska and British Columbia: Geological Society of America Bulletin, v. 106, no. 5, p. 715–728, https://doi.org/10.1130/0016-7606(1994)106<0715:TGTSEI>2.3.CO;2.

Israel, S.A., 2008, Tectonic Significance of the Atnarko Complex, Coast Mountains, British Columbia [Ph.D. thesis]: Vancouver, British Columbia, Canada, University of British Columbia, 192 p. with maps and figures.

Israel, S.A., Schiarizza, P., Kennedy, L.A., Friedman, R.M., and Villeneuve, M., 2006, Evidence for Early to Late Cretaceous sinistral deformation in the Tchaikazan River area, southwestern British Columbia: Implications for the tectonic evolution of the southern Coast belt, *in* Haggart, J.W., Enkin, R.J., and Monger, J.W.H., eds., Paleogeography of the North American Cordillera: Evidence For and Against Large-Scale Displacements: Geological Association of Canada Special Paper 46, p. 331–350.

Israel, S.A., Kennedy, L.A., and Friedman, R.M., 2013, Strain partitioning in accretionary orogens, and its effects on orogenic collapse: Insights from western North America: Geological Society of America Bulletin, v. 125, no. 7–8, p. 1260–1281, https://doi.org/10.1130/B30777.1.

Jaffey, A.H., Flynn, K.F., Glendenin, L.E., Bentley, W.C., and Essling, A.M., 1971, Precision measurement of half-lives and specific activities of ^{235}U and ^{238}U: Physical Review C, v. 4, no. 5, p. 1889, https://doi.org/10.1103/PhysRevC.4.1889.

Journeay, J., and Friedman, R., 1993, The Coast belt thrust system: Evidence of Late Cretaceous shortening in southwest British Columbia: Tectonics, v. 12, no. 3, p. 756–775, https://doi.org/10.1029/92TC02773.

Kapp, P.A., and Gehrels, G.E., 1998, Detrital zircon constraints on the tectonic evolution of the Gravina belt, southeastern Alaska: Canadian Journal of Earth Sciences, v. 35, no. 3, p. 253–268, https://doi.org/10.1139/e97-110.

Klepeis, K.A., Crawford, M.L., and Gehrels, G., 1998, Structural history of the crustal-scale Coast shear zone north of Portland Canal, southeast Alaska and British Columbia: Journal of Structural Geology, v. 20, no. 7, p. 883–904, https://doi.org/10.1016/S0191-8141(98)00020-0.

Lin, S., Jiang, D., and Williams, P.F., 1998, Transpression (or transtension) zones of triclinic symmetry: Natural example and theoretical modelling, *in* Holdsworth, R.E., Strachan, R.A., and Dewey, J.F., eds., Continental Transpressional and Transtensional Tectonics: Geological Society, London, Special Publication 135, p. 41–57, https://doi.org/10.1144/GSL.SP.1998.135.01.04.

Matthews, W.A., Guest, B., Coutts, D., Bain, H., and Hubbard, S., 2017, Detrital zircons from the Nanaimo basin, Vancouver Island, British Columbia: An independent test of Late Cretaceous to Cenozoic northward translation: Tectonics, v. 36, no. 5, p. 854–876, https://doi.org/10.1002/2017TC004531.

McClelland, W.C., and Gehrels, G.E., 1990, Geology of the Duncan Canal shear zone: Evidence for Early to Middle Jurassic deformation of the Alexander terrane, southeastern Alaska: Geological Society of America Bulletin, v. 102, no. 10, p. 1378–1392, https://doi.org/10.1130/0016-7606(1990)102<1378:GOTDCS>2.3.CO;2.

McClelland, W.C., Gehrels, G.E., Samson, S.D., and Patchett, P.J., 1992, Structural and geochronologic relations along the western flank of the Coast Mountains Batholith: Stikine River to Cape Fanshaw, central southeastern Alaska: Journal of Structural Geology, v. 14, no. 4, p. 475–489, https://doi.org/10.1016/0191-8141(92)90107-8.

McGroder, M.F., 1991, Reconciliation of two-sided thrusting, burial metamorphism, and diachronous uplift in the Cascades of Washington and British Columbia: Geological Society of America Bulletin, v. 103, no. 2, p. 189–209, https://doi.org/10.1130/0016-7606(1991)103<0189:ROTSTB>2.3.CO;2.

Merdith, A.S., Williams, S.E., Collins, A.S., Tetley, M.G., Mulder, J.A., Blades, M.L., Young, A., Armistead, S.E., Cannon, J., and Zahirovic, S., 2020, Extending full-plate tectonic models into deep time: Linking the Neoproterozoic and the Phanerozoic: Earth-Science Reviews, v. 214, https://doi.org/10.1016/j.earscirev.2020.103477.

Miller, I.M., Brandon, M.T., and Hickey, L.J., 2006, Using leaf margin analysis to estimate the mid-Cretaceous (Albian) paleolatitude of the Baja BC block: Earth and Planetary Science Letters, v. 245, no. 1–2, p. 95–114, https://doi.org/10.1016/j.epsl.2006.02.022.

Miller, J.S., Matzel, J.E., Miller, C.F., Burgess, S.D., and Miller, R.B., 2007, Zircon growth and recycling during the assembly of large, composite arc plutons: Journal of Volcanology and Geothermal Research, v. 167, no. 1–4, p. 282–299, https://doi.org/10.1016/j.jvolgeores.2007.04.019.

Mahoney, J.B., Mustard, P.S., Haggart, J.W., Friedman, R.M., Fanning, M.C., and McNicoll, V.J., 1999, Archean zircons in Cretaceous strata of the western Canadian Cordillera: The "Baja BC" hypothesis fails a "crucial test": Geology, v. 27, no. 3, p. 195–198, https://doi.org/10.1130/0091-7613(1999)027%3C0195:AZICSO%3E2.3.CO;2.

Monger, J.W.H., Price, R.A., and Tempelman-Kluit, D.J., 1982, Tectonic accretion and the origin of the two major metamorphic and plutonic welts in the Canadian Cordillera: Geology, v. 10, p. 70–75, https://doi.org/10.1130/0091-7613(1982)10%3C70:TAATOO%3E2.0.CO;2.

Monger, J.W.H., 2014, Logan Medallist 1. Seeking the suture: The Coast-Cascade conundrum: Geoscience Canada: Journal of the Geological Association of Canada/Geoscience Canada, v. 41, no. 4, p. 379–398, https://doi.org/10.12789/geocanj.2014.41.058.

Monger, J.W.H., and Gibson, H.D., 2019, Mesozoic–Cenozoic deformation in the Canadian Cordillera: The record of a "continental bulldozer"?: Tectonophysics, v. 757, p. 153–169, https://doi.org/10.1016/j.tecto.2018.12.023.

Monger, J.W.H., Price, R.A., and Tempelman-Kluit, D.J., 1982, Tectonic accretion and the origin of the two major metamorphic and plutonic welts in the Canadian Cordillera: Geology, v. 10, no. 2, p. 70–75, https://doi.org/10.1130/0091-7613(1982)10<70:TAATOO>2.0.CO;2.

Monger, J.W.H., Van der Heyden, P., Journeay, J., Evenchick, C., and Mahoney, J., 1994, Jurassic–Cretaceous basins along the Canadian Coast belt: Their bearing on pre–mid-Cretaceous sinistral displacements: Geology, v. 22, no. 2, p. 175–178, https://doi.org/10.1130/0091-7613(1994)022<0175:JCBATC>2.3.CO;2.

Monger, J.W.H., Struik, L., Haggart, J., and Enkin, R., 2006, Chilliwack terrane: A slice of Stikinia? A tale of terrane transfer, *in* Haggart, J.W., Enkin, R.J., and Monger, J.W.H., eds., Paleogeography of the North American Cordillera: Evidence For and Against Large-Scale Displacements: Geological Association of Canada Special Paper 46, p. 351–368.

Moser, A.C., Hacker, B.R., Gehrels, G.E., Seward, G.G., Kylander-Clark, A.R., and Garber, J.M., 2022, Linking titanite U-Pb dates to coupled deformation and dissolution-reprecipitation: Contributions to Mineralogy and Petrology, v. 177, no. 3, p. 1–27, https://doi.org/10.1007/s00410-022-01906-9.

Müller, R.D., Seton, M., Zahirovic, S., Williams, S.E., Matthews, K.J., Wright, N.M., Shephard, G.E., Maloney, K.T., Barnett-Moore, N., and Hosseinpour, M., 2016, Ocean basin

evolution and global-scale plate reorganization events since Pangea breakup: Annual Review of Earth and Planetary Sciences, v. 44, p. 107–138, https://doi.org/10.1146/annurev-earth-060115-012211.

Nelson, J., Diakow, L., Karl, S., Mahoney, J., Gehrels, G., Pecha, M., and van Staal, C., 2011, Geology and mineral potential of the southern Alexander terrane and western Coast plutonic complex near Klemtu, northwestern British Columbia: Geological Fieldwork 2010: British Columbia Ministry of Energy and Mines Paper 2011-1, p. 73–97.

Nelson, J., Diakow, L., Mahoney, J., van Staal, C., Pecha, M., Angen, J., Gehrels, G., and Lau, T., 2012, North Coast project: Tectonics and metallogeny of the Alexander terrane, and Cretaceous sinistral shearing of the western Coast belt: Geological Fieldwork 2011: British Columbia Ministry of Energy and Mines Paper 2012-1, p. 157–180.

Nelson, J., Diakow, L., Mahoney, B., Gehrels, G., van Staal, C., Karl, S., Pecha, M., and Angen, J., 2014, Geology of the North and Mid-Coast Regions, British Columbia: British Columbia Geological Survey Geoscience Map/Open-File 2014–3 (2 sheets), scale 1:150,000, https://doi.org/10.4095/295460.

Neves, S., Vauchez, A., and Archanjo, C., 1996, Shear zone–controlled magma emplacement or magma-assisted nucleation of shear zones? Insights from northeast Brazil: Tectonophysics, v. 262, no. 1–4, p. 349–364, https://doi.org/10.1016/0040-1951(96)00007-8.

Paces, J.B., and Miller, J.D., Jr., 1993, Precise U-Pb ages of Duluth complex and related mafic intrusions, northeastern Minnesota: Geochronological insights to physical, petrogenetic, paleomagnetic, and tectonomagmatic processes associated with the 1.1 Ga Midcontinent rift system: Journal of Geophysical Research–Solid Earth, v. 98, p. 13,997–14,013, https://doi.org/10.1029/93JB01159.

Paterson, S.R., Vernon, R.H., and Tobisch, O.T., 1989, A review of criteria for the identification of magmatic and tectonic foliations in granitoids: Journal of Structural Geology, v. 11, no. 3, p. 349–363, https://doi.org/10.1016/0191-8141(89)90074-6.

Pavlis, T.L., Amato, J.M., Trop, J.M., Ridgway, K.D., Roeske, S.M., and Gehrels, G.E., 2019, Subduction polarity in ancient arcs: A call to integrate geology and geophysics to decipher the Mesozoic tectonic history of the Northern Cordillera of North America: GSA Today, v. 29, no. 11, p. 4–10, https://doi.org/10.1130/GSATG402A.1.

Pearson, J., and Hebda, R.J., 2006, Paleoclimate of the Late Cretaceous Cranberry Arms flora of Vancouver Island: Evidence for latitudinal displacement, *in* Haggart, J., Enkin, R.J., and Monger, J.W.H., eds., Paleogeography of the North American Cordillera: Evidence For and Against Large-Scale Displacements: Geological Association of Canada Special Paper 46, p. 133–145.

Plafker, G., and Berg, H.C., 1994, Overview of the geology and tectonic evolution of Alaska, *in* Plafker, G., and Berg, H.C., eds., The Geology of Alaska: Boulder, Colorado, Geological Society of America, The Geology of North America, v. G-1, p. 989–1021, https://doi.org/10.1130/DNAG-GNA-G1.989.

Plafker, G., Nokleberg, W.J., and Lull, J., 1989, Bedrock geology and tectonic evolution of the Wrangellia, Peninsular, and Chugach terranes along the Trans-Alaska Crustal Transect in the Chugach Mountains and southern Copper River Basin, Alaska: Journal of Geophysical Research–Solid Earth, v. 94, p. 4255–4295, https://doi.org/10.1029/JB094iB04p04255.

Rubin, C.M., Saleeby, J.B., Cowan, D.S., Brandon, M.T., and McGroder, M.F., 1990, Regionally extensive mid-Cretaceous west-vergent thrust system in the northwestern Cordillera: Implications for continent-margin tectonism: Geology, v. 18, no. 3, p. 276–280, https://doi.org/10.1130/0091-7613(1990)018<0276:REMCWV>2.3.CO;2.

Rusmore, M.E., and Woodsworth, G., 1991, Distribution and tectonic significance of Upper Triassic terranes in the eastern Coast Mountains and adjacent Intermontane belt, British Columbia: Canadian Journal of Earth Sciences, v. 28, no. 4, p. 532–541, https://doi.org/10.1139/e91-047.

Rusmore, M.E., and Woodsworth, G., 1994, Evolution of the eastern Waddington thrust belt and its relation to the mid-Cretaceous Coast Mountains arc, western British Columbia: Tectonics, v. 13, no. 5, p. 1052–1067, https://doi.org/10.1029/94TC01316.

Rusmore, M.E., Gehrels, G., and Woodsworth, G.J., 2001, Southern continuation of the Coast shear zone and Paleocene strain partitioning in British Columbia–southeast Alaska: Geological Society of America Bulletin, v. 113, no. 8, p. 961–975, https://doi.org/10.1130/0016-7606(2001)113<0961:SCOTCS>2.0.CO;2.

Rusmore, M.E., Bogue, S.W., and Woodsworth, G.J., 2013, Paleogeography of the Insular and Intermontane terranes reconsidered: Evidence from the southern Coast Mountains Batholith, British Columbia: Lithosphere, v. 5, no. 5, p. 521–536, https://doi.org/10.1130/L288.1.

Schiarizza, P., Gaba, R., Glover, J., Garver, J., and Umhoefer, P., 1997, Geology and Mineral Occurrences of the Taseko-Bridge River Area: British Columbia Ministry of Employment and Investment, Geological Survey Branch Bulletin 100, p. 195–199.

Sigloch, K., and Mihalynuk, M.G., 2013, Intra-oceanic subduction shaped the assembly of Cordilleran North America: Nature, v. 496, no. 7443, p. 50–56, https://doi.org/10.1038/nature12019.

Sigloch, K., and Mihalynuk, M.G., 2017, Mantle and geological evidence for a Late Jurassic–Cretaceous suture spanning North America: Geological Society of America Bulletin, v. 129, no. 11–12, p. 1489–1520, https://doi.org/10.1130/B31529.1.

Sundell, K.E., Gehrels, G.E., and Pecha, M.E., 2021, Rapid U-Pb geochronology by laser ablation multi-collector ICP-MS: Geostandards and Geoanalytical Research, v. 45, no. 1, p. 37–57, https://doi.org/10.1111/ggr.12355.

Tikoff, B., and Greene, D., 1997, Stretching lineations in transpressional shear zones: An example from the Sierra Nevada Batholith, California: Journal of Structural Geology, v. 19, no. 1, p. 29–39, https://doi.org/10.1016/S0191-8141(96)00056-9.

Tikoff, B., and Teyssier, C., 1994, Strain modeling of displacement-field partitioning in transpressional orogens: Journal of Structural Geology, v. 16, no. 11, p. 1575–1588, https://doi.org/10.1016/0191-8141(94)90034-5.

Tochilin, C.J., Gehrels, G.E., Nelson, J., and Mahoney, J.B., 2014, U-Pb and Hf isotope analysis of detrital zircons from the Banks Island assemblage (coastal British Columbia) and southern Alexander terrane (southeast Alaska): Lithosphere, v. 6, no. 3, p. 200–215, https://doi.org/10.1130/L338.1.

Umhoefer, P.J., 2003, A model for the North America Cordillera in the Early Cretaceous: Tectonic escape related to arc collision of the Guerrero terrane and a change in North America plate motion, *in* Johnson, S.E., Paterson, S.R., Fletcher, J.M., Girty, G.H., Kimbrough, D.L., and Martín-Barajas, A., eds., Tectonic Evolution of Northwestern Mexico and the Southwestern USA: Geological Society of America Special Paper 364, p. 117–134, https://doi.org/10.1130/0-8137-2374-4.117.

Umhoefer, P.J., Schiarizza, P., and Robinson, M., 2002, Relay Mountain Group, Tyaughton Methow basin, southwest British Columbia: A major Middle Jurassic to Early Cretaceous terrane overlap assemblage: Canadian Journal of Earth Sciences, v. 39, no. 7, p. 1143–1167, https://doi.org/10.1139/e02-031.

Umhoefer, P.J., Blakey, R.C., Haggart, J., Enkin, R., and Monger, J., 2006, Moderate (1600 km) northward translation of Baja British Columbia from southern California: An attempt at reconciliation of paleomagnetism and geology, *in* Haggart, J.W., Enkin, R.J., and Monger, J.W.H., eds., Paleogeography of the North American Cordillera: Evidence For and Against Large-Scale Displacements: Geological Association of Canada Special Paper 46, p. 307–329.

van der Heyden, P., 1992, A Middle Jurassic to early Tertiary Andean-Sierran arc model for the Coast belt of British Columbia: Tectonics, v. 11, no. 1, p. 82–97, https://doi.org/10.1029/91TC02183.

Vermeesch, P., 2018, IsoplotR: A free and open toolbox for geochronology: Geoscience Frontiers, v. 9, no. 5, p. 1479–1493, https://doi.org/10.1016/j.gsf.2018.04.001.

Wendt, I., and Carl, C., 1991, The statistical distribution of the mean squared weighted deviation: Chemical Geology–Isotope Geoscience Section, v. 86, no. 4, p. 275–285, https://doi.org/10.1016/0168-9622(91)90010-T.

Wheeler, J.O., and McFeely, P., 1991, Tectonic Assemblage Map of the Canadian Cordillera and Adjacent Parts of the United States of America: Geological Survey of Canada "A" Series Map 1712A, 2 sheets, https://doi.org/10.4095/133549.

Wolf, D.E., Andronicos, C.L., Vervoort, J.D., Mansfield, M.R., and Chardon, D., 2010, Application of Lu-Hf garnet dating to unravel the relationships between deformation, metamorphism and plutonism: An example from the Prince Rupert area, British Columbia: Tectonophysics, v. 485, no. 1–4, p. 62–77, https://doi.org/10.1016/j.tecto.2009.11.020.

Wyld, S.J., Umhoefer, P.J., Wright, J.E., Haggart, J., Enkin, R., and Monger, J., 2006, Reconstructing northern Cordilleran terranes along known Cretaceous and Cenozoic strike-slip faults: Implications for the Baja British Columbia hypothesis and other models, *in* Haggart, J.W., Enkin, R.J., and Monger, J.W.H., eds., Paleogeography of the North American cordillera: Evidence for and against large-scale displacements: Geological Association of Canada Special Paper 46, p. 277–298.

Yokelson, I., Gehrels, G.E., Pecha, M., Giesler, D., White, C., and McClelland, W.C., 2015, U-Pb and Hf isotope analysis of detrital zircons from Mesozoic strata of the Gravina belt, southeast Alaska: Tectonics, v. 34, no. 10, p. 2052–2066, https://doi.org/10.1002/2015TC003955.